EUROPEAN ORGANIZATION FOR NUCLEAR RESEARCH

CERN-EP/79-146
21 November 1979

JET-LIKE STRUCTURE IN THE REACTION $\gamma p \to \pi^+\pi^-\pi^+\pi^-\pi^+\pi^- p$

Bonn[1]-CERN[2]-Ecole Polytechnique[3]-Glasgow[4]-Lancaster[5]-Manchester[6]-
Orsay[7]-Paris VI[8]-Paris VII[9]-Rutherford[10]-Sheffield[11] Collaboration

D. Aston[10], M. Atkinson[10], R. Bailey[11], A.H. Ball[6], B. Bouquet[7],
G.R. Brookes[11], J. Bröring[1], P.J. Bussey[4], D. Clarke[10], A.B. Clegg[5],
B. d'Almagne[7], G. de Rosny[3], B. Diekmann[1], A. Donnachie[6],
M. Draper[4], B. Drevillon[3], I.P. Duerdoth[6], J.-P. Dufey[2],
R.J. Ellison[6], D. Ezra[6], P. Feller[1], A. Ferrer[7], P.J. Flynn[5],
F. Friese[1], W. Galbraith[11], R. George[8], S.D.M. Gill[6], M. Goldberg[8],
S. Goodman[8], W. Graves[3], B. Grossetête[9], P.G. Hampson[6],
K. Heinloth[1], R.E. Hughes-Jones[6], J.S. Hutton[10], M. Ibbotson[6], M. Jung[1],
S. Katsanevas[3], M.A.R. Kemp[10], F. Kovacs[9], B.R. Kumar[10], G.D. Lafferty[5],
J.B. Lane[6], J.-M. Lévy[8], V. Liebenau[1], J. Litt[10], G. London[8], D. Mercer[6],
J.V. Morris[10], K. Müller[1], D. Newton[5], E. Paul[1], P. Petroff[7], Y. Pons[9], C. Raine[11],
F. Richard[7], R. Richter[1], J.H.C. Roberts[6], P. Roudeau[7], A. Rougé[3], M. Rumpf[3],
M. Sené[8], J. Six[7], I.O. Skillicorn[4], J.C. Sleeman[4], K.M. Smith[4], C. Steinhauer[1],
K.M. Storr[5], R.J. Thompson[6], D. Treille[2], Ch. de la Vaissière[8], H. Videau[3],
I. Videau[3], A.P. Waite[6], A. Wijangco[3], W. Wojcik[7*], J.-P. Wuthrick[3], T.P. Yiou[8]

(Submitted to Nuclear Physics B)

---

* On leave of absence from University of Warsaw, Warsaw, Poland.

ABSTRACT

We report on diffractive production of 6π systems with a continuum of masses from 2 to 5 GeV/c^2 in the reaction $\gamma p \to \pi^+\pi^-\pi^+\pi^-\pi^+\pi^- p$. The event structure is compared in detail with Monte Carlo studies of p_T-limited phase space, and with the jets observed in hadronic systems produced by electron-positron annihilation. Strong similarities are found. For this jet-like structure of the 6π system the axis is consistent with being along the incident photon direction.

1. INTRODUCTION

We discuss the characteristics of the reaction

$$\gamma p \rightarrow \pi^+\pi^-\pi^+\pi^-\pi^+\pi^- p \qquad (1)$$

for incident photon energies from 25 to 70 GeV. In particular we study diffractively produced $\pi^+\pi^-\pi^+\pi^-\pi^+\pi^-$ systems of masses from 2 to 5 GeV/c^2. A study of diffractive processes is of interest because diffractive dissociation of the photon has provided a means of studying the hadronic content of the photon. Previous experiments have demonstrated [1] that a large fraction of the photon cross-section is due to ρ, ω and ϕ mesons. However a continuum of higher mass states is also expected to contribute [2] and could be observed in reaction (1). Another motivation for studying this reaction is the suggestion that the increase in γp cross-section over that due to vector meson dominance may be due to the production of high transverse momentum jets.

We have chosen to study reaction (1) because its multiplicity permits a detailed jet analysis to be made. A channel involving only charged particles was chosen to reduce experimental uncertainties and to maximize experimental acceptance.

We observe a structureless 6π mass spectrum. The 6π system is well described by transverse momentum limited phase space, and this forms an apparent two-jet system. The axes of the jets are aligned along the beam direction. The structure of the jet is similar to that found in electron-positron annihilation.

2. EXPERIMENTAL DETAILS

2.1 The electron beam

Protons of 210 GeV energy from the CERN Super Proton Synchrotron (SPS) struck a beryllium target. The resulting charged particles were swept out by a magnetic field, while gamma-rays (and neutrons) struck a lead converter of thickness 0.5 radiation lengths, where the gamma-rays produced electrons. A conventional

beam line selected and transported electrons of a mean momentum of 81.5 GeV/c to the tagging system. A typical electron flux was 2×10^6 per spill of $\sim$ 1 sec, for a momentum bite of ±2%.

2.2 Photon tagging system

The tagging system is shown schematically in fig. 1. The electrons produced photons in a tungsten radiator of thickness 0.076 radiation lengths. The energy of each photon was deduced from measurements of the incident and scattered electron momenta. The incident electron momentum was determined from the 68 mrad deflection in the last bend of the beam line. The precise deflection was determined from trajectories measured in two systems of multiwire proportional chambers placed before and after the bend. Each of these systems extended over 7 m and was made up of four sets of four planes, with each set of four planes having wires at 0°, 45°, 90°, and 135° to the vertical. The large number of planes allowed reconstruction of tracks even in the presence of background tracks or of depressed chamber efficiencies due to high instantaneous beam rates. The scattered electrons passed through a further system of multiwire proportional chambers, counter hodoscopes and lead-glass counters, which accepted scattered electrons with momenta from 10 to 60 GeV/c. Their trajectories were determined by 6 planes of multiwire proportional chambers with wires inclined at 0° or 60° to the vertical. These were followed by two planes of scintillation counter hodoscopes, which were used in the trigger, and then by a hodoscope of 56 lead-glass blocks, whose pulse-height provided a final check on the correct identification of the particles as electrons. The tagging system was completed by various veto counters placed downstream of the radiator to reject events in which more complicated processes such as multiple bremsstrahlung took place, or when the photon was off axis.

2.3 Detection system

The Omega detection system, as equipped for this experiment, is shown schematically in fig. 2. The photon was close to collinear with the incident

electron, which enabled the photon beam to be effectively focused on the centre of the hydrogen target, which was 25 mm in radius and 670 mm in length. The target and charged particle detectors were placed in the magnet of the Omega spectrometer which provided a field, in this experiment, of 0.9 T over a volume of radius $\sim$ 2 m and height 1.5 m. The primary particle detectors were spark chambers comprising a forward detector of 7 modules each of 10 gaps, and two side detectors each of 4 modules of 8 gaps. The spark chambers were complemented by other detectors:

i) A detector surrounding the target, formed by the combination of a multiwire proportional chamber, with wires spaced at 0.5 mm over an active area of 40 mm radius, placed at the downstream end of the target and a cylindrical hodoscope, surrounding the sides of the target, made up of 24 scintillation counters aligned along the length of the target. This detector was used in the trigger.

ii) Three further multiwire proportional counter systems, distributed downstream of the target. These were used in the trigger and to aid pattern recognition.

iii) Two large drift chamber modules, each of four planes, placed downstream of the magnetic field region. They provided precise measurements of points on particle trajectories which both aided pattern recognition and gave considerable improvement in momentum resolution for higher momentum tracks.

iv) A large threshold Čerenkov counter filled with carbon dioxide at atmospheric pressure, following the drift chambers. The threshold momenta which we used for identification were $\sim$ 5.9 GeV/c for pions and $\sim$ 19 GeV/c for kaons. Almost all particles produced with momenta greater than 5.9 GeV/c passed through this counter.

v) A large photon detector, following the Čerenkov detector. The information from this photon detector is not used in the present paper.

2.4 Trigger

The trigger used in the present work required a forward multiplicity between 4 and 9, which eliminated most of the electromagnetic background. In detail, there were four components of the trigger:

i) A signal from the tagging system, indicating the production of an incident photon of energy between 20 and 70 GeV.

ii) A signal from the detector around the target, indicating that 4 or more particles had been detected in it.

iii) Signals from two planes of a multiwire proportional chamber system of area 1.5 m × 1 m placed 1.5 m downstream from the centre of the target. One of these planes, with vertical wires, was required to have detected M charged particles where $3 \leq M \leq 9$, while the other, with horizontal wires, was required to have detected N charged particles where $4 \leq N \leq 9$.

iv) A signal from a further multiwire proportional chamber system downstream requiring there to be at least one particle produced in a region away from the median plane. This requirement further reduced the background due to electromagnetic processes.

This trigger produced an event rate corresponding to a cross-section of about 70 μb. About 20% of the triggers were due to electromagnetic processes.

2.5 Data taking and data analysis

A total of 6×10^6 triggers of the type described in Section 2.4 were recorded. These data were passed successively through three analysis programs:

i) A fast pattern recognition program which identified high momentum tracks from hits in the drift chambers and multiwire proportional chambers. Some events with tracks only in the median plane were rejected at this stage as electromagnetic background. Tracks with momentum greater than 5.9 GeV/c and with no signal from the Čerenkov counter were identified as kaons, or

as protons if above 19 GeV/c. The data were then divided into two categories: one containing those events with one or more particles identified as a kaon or proton, and the other with no such particles. Only events in the latter category were used in the present work.

ii) The ROMEO program [3], which does pattern recognition and geometrical reconstruction for tracks in the Omega spectrometer. In the version used in this experiment pattern recognition was improved by information passed on from the fast pattern recognition program.

iii) A further program which received the output of the ROMEO program, analysed the photon tagging system and Čerenkov counter information, and produced data summary tapes.

About half the data from the non-kaon category have been used in the present work.

3. SELECTION OF EVENTS

In our study of the reaction

$$\gamma p \rightarrow \pi^+ \pi^- \pi^+ \pi^- \pi^+ \pi^- p$$

the recoil proton was detected in approximately 30% of the events. This was due to the low momentum of the proton and to the incomplete geometrical coverage of the side spark chambers. We therefore accepted events in which three negative tracks and either three or four positive tracks were detected. For events in which 6 particles were detected we took them all to be pions, while for the events with 7 detected particles we assumed the positive particle which had the smallest longitudinal momentum, with respect to the beam, to be the proton and took the other six particles to be pions. In this latter case we only accepted the event if the apparent proton had a momentum less than 1 GeV/c. The treatment of this data sample required the solution of two problems discussed in Sections 3.1 and 3.2.

3.1 Separation of elastic sample

We require to select events such that when 6 particles are observed only a recoil proton is missing and when 7 particles are observed there are no missing particles. For each event we calculated the variable:

ΔE = Incident beam energy - sum of pion energies
- proton kinetic energy (when the proton is observed).

In principle, a distribution of measurements of ΔE should show a peak at $\Delta E = 0$ for elastic events, and a distribution with $\Delta E > 0$ for inelastic events (events with missing particles). In practice, owing to our limited energy resolution, these distributions overlap, as shown in fig. 3. To separate elastic and inelastic events further investigation was needed. This was possible when 7 particles were observed, and for those events we studied the distribution of components of total observed momentum transverse to the beam. Each component of this transverse momentum gave rise to two quite distinct but superimposed distributions: one with FWHM ≈ 0.06 GeV/c, assumed due to elastic events, and the other with FWHM ≈ 0.8 GeV/c, assumed due to inelastic events. From the intensities of these two distributions as a function of ΔE we determined the numbers of elastic and inelastic events as a function of ΔE for events with 7 observed particles. The curve in fig. 3 corresponds to inelastic events from this sample. We assume that the shape of the distribution for inelastic events is the same function of ΔE for events with 6 observed particles. The difference between the data points and the curve in fig. 3 then indicates the peak in the region $\Delta E \approx 0$ due to elastic events of reaction (1).

The conclusion of this study was that a cut on ΔE from -1.4 to +0.6 GeV makes a suitable selection of elastic events. The fraction of inelastic contamination varied with photon energy: for 6π masses between 2 and 4 GeV/c^2 we found that this fraction falls from $\sim 1/3$ at $E_\gamma = 35$ GeV to $\sim 1/5$ at $E_\gamma = 70$ GeV.

3.2 Proton identification

Slow recoil protons could not be identified event-by-event, since they overlapped in momentum and angle with slow pions, especially for high mass events. Hence we selected protons as described above and analysed events only in regions of 6π mass and photon energy such that the proton identification is satisfactory. To find these regions we have used our observation that the 6π system is well described by p_T-limited phase space, and have generated Monte-Carlo events with this characteristic. Specifically we generated

$$X \rightarrow \pi^+\pi^-\pi^+\pi^-\pi^+\pi^-$$

for various masses of X, assuming the pions are distributed according to phase space weighted by $\Pi_{i=1}^{6} \exp(-Ap_{Ti})$, where p_{Ti} is the transverse momentum of the pions with respect to an axis. The values A = 3.0 for M < 3.5 GeV/c^2, and A = 3.5 for M > 3.5 GeV/c^2, were found to give the best correspondence with the experimental data. We then generated $\gamma p \rightarrow Xp$, aligning the axis with the beam and giving the reaction a distribution of $\exp(-6p_T)$, where p_T now denotes the transverse momentum of the proton with respect to the beam.

Monte Carlo generated events were subjected to the same analysis procedure as our experimental data. This provided a measure of the reliability of the proton identification procedure described above. It was found that for events with the range of mass and photon energy given in table 1 the fraction of events with proton misidentification was less than 25%. It was also found from these Monte Carlo studies that event selection according to these limits would correspond to good experimental acceptance as shown in fig. 4. Event selection according to table 1 was therefore adopted for the experimental data.

4. PRODUCTION OF 6π SYSTEM

We have divided our experimental data according to three ranges of incident photon energy: 25-35, 35-50, and 50-70 GeV. The experimental 6π mass spectrum corresponding to each range is shown in fig. 5. These spectra are uncorrected

for effects of acceptance and biases introduced by the proton identification procedure. We remark only that they are structureless, and show little or no dependence on incident photon energy apart from kinematics.

In Section 3.2 we described a procedure by which we generated Monte Carlo events with the characteristic of p_T limited phase space for the 6π system. For comparison we also generated Monte Carlo events for $\gamma p \to 6\pi p$, in which the seven final-state particles were distributed according to phase space weighted by $\Pi_{i=1}^{7} \exp(-Ap_{Ti})$. Such models produce only a small proportion of events within the limits of table 1, indicating that the contamination from central collision processes is small in our data.

In order to make a quantitative estimate of the energy dependence of the cross-section, we have studied a region of mass and photon energy where proton identification and acceptance are good, as deduced in Section 3.2. The 6π mass range 2-4 GeV/c^2 was chosen and consequently photon energies greater than 35 GeV. We found that the magnitude of the cross-section for producing these 6π states was approximately 0.1 μb, falling only by the factor 0.9 ± 0.2 from incident photon energy 35-50 GeV to incident photon energy 50-70 GeV. This constant cross-section is suggestive of diffractive dissociation of the photon, producing a smooth mass spectrum up to masses $0.45\sqrt{s}$. Masses up to a similar fraction of the available energy have been attributed to diffractive dissociation in other high-energy reactions [4,5]. Our t-distributions, fig. 6, also have slopes (table 2) similar to those found in diffractive dissociation processes producing high mass states in other reactions [4]. We therefore conclude that, with the event selection described above, diffractive dissociation of the photon is a major contributor to the reaction channel (1).

Rho-meson production is not dominant in these events. The mass spectrum for $\pi^+\pi^-$ combinations is shown in fig. 7a and for $\pi^+\pi^+$ and $\pi^-\pi^-$ combinations is shown in fig. 7b. The ρ^0 meson peak in fig. 7a corresponds to approximately 0.5 ρ^0 meson/event, which means the $\rho^0/\pi^{\pm}$ ratio is approximately 0.1.

5. STRUCTURE OF 6π SYSTEM

The six pions produced by diffractive dissociation of the photon can be regarded as the products of a photon-Pomeron collision. Therefore we took as a polar axis the direction of the photon in the 6π c.m. system, and examined the distributions of momenta and charges with respect to this axis. We shall show that the experimental results are well described by p_T-limited phase space relative to this axis.

To establish this conclusion we compared our data with results of Monte Carlo calculations; we generated

$$X \to \pi^+\pi^-\pi^+\pi^-\pi^+\pi^-$$

for a fixed mass, with the pions distributed according to phase space weighted by $\Pi_{i=1}^{6} \exp(-Ap_{Ti})$. Our comparisons have been for calculations with $A = 3.0\ (GeV/c)^{-1}$ for masses $< 3.5\ GeV/c^2$ and with $A = 3.5$ for masses $> 3.5\ GeV/c^2$. The agreement between these Monte Carlo distributions and our experimental p_T distributions was good. A typical comparison, for one mass range and for three regions of Feynman x, is given in fig. 8. It was found that Monte Carlo simulation with phase space weighted with $\Pi_{i=1}^{6} \exp(-Bp_{Ti}^2)$ did not produce agreement with the experimental p_T distributions, even for a value of B which simulated adequately the mean value $\langle p_T \rangle$. An example of this poor agreement is the broken curve in fig. 8 calculated for $B = 4.5\ (GeV/c)^{-2}$.

The structure of the 6π system will now be described in terms of the mean p_T, the rapidity and x distributions, and the charge distributions and correlations. In each case we studied dependence on the 6π mass M and photon energy E_γ over the ranges specified in table 1. We found dependence on M, but not on E_γ. This result is consistent with what would be expected from production of the 6π system by an exchange process, such as occurs in diffractive dissociation of the photon, and also with p_T-limited phase space for $\gamma p \to 6\pi p$.

5.1 $\langle p_T \rangle$ as a function of 6π mass

These results are summarized in fig. 9, where we show, as a function of 6π mass, the average values of p_T

$$\langle p_T \rangle = \frac{1}{N} \sum p_T ,$$

where the summation runs over all the pions from the 6π systems selected, N is the total number of pions, and p_T is the component of the pion's momentum transverse to the incident photon direction in the 6π c.m. system. We see that though $\langle p_T \rangle$ rises slowly with 6π mass, it is, for masses > 2.5 GeV/c^2, much less than is calculated for isotropic phase space. In fig. 9 we also show calculated variations of $\langle p_T \rangle$ for phase space weighted by $\Pi_{i=1}^{6} \exp(-Ap_{Ti})$ and with $\Pi_{i=1}^{6} \exp(-Bp_{Ti}^2)$. We see that our results are in good agreement with the data for $A \approx 3.0$–3.5. The agreement for $B = 4.5$ is satisfactory for $\langle p_T \rangle$, but as already noted the distributions of fig. 8 are not well reproduced with this weighting factor.

5.2 Distribution in rapidity and in Feynman x

Figure 10 shows the distributions of particles as a function of longitudinal rapidity in the 6π c.m. system. We note that as the mass of the 6π system increases, a rapidity plateau develops as expected from p_T-limited phase space.

Figure 11 shows the distributions as a function of Feynman x, where we have taken

$$x = p_L / p_{Lmax} ,$$

and where p_{Lmax} is the maximum possible pion momentum for the event of mass M, calculated from

$$E_{max} = (M^2 - 24\mu^2)/2M .$$

Here μ is the pion mass. The results indicate rather good agreement with Feynman scaling, and there is also good agreement with p_T-limited phase space as is shown by the calculated curves.

In both figs. 10 and 11, there is forward-backward symmetry in the 6π c.m. system. This is interesting since a photon-Pomeron collision does not necessarily have such symmetry.

5.3 $\langle p_T \rangle$ as a function of Feynman x

The variation of $\langle p_T \rangle$ as a function of x for various 6π mass ranges is shown in fig. 12. One notes again the rise in $\langle p_T \rangle$ with mass, already seen in fig. 9, and the development of a "seagull" dip at x = 0, especially at large 6π mass. The data indicate also a possible small departure from forward-backward symmetry.

In the literature the seagull effect has been attributed to [6-8]

i) an effect of p_T-limited phase space,

ii) a kinematic effect from meson resonances,

iii) an effect of mixed final-state multiplicities,

iv) dynamical effects of quark dressing.

In our data there is a unique multiplicity. There is no contribution from ω^0 and η^0 meson resonances, and we found that the small ρ^0 contribution already mentioned results in *both* its decay pions lying outside the small x and small p_T region. Since it is the large number of pions with $|x| < 0.1$ and $p_T < 0.3$ GeV/c which cause the seagull effect, we conclude that neither ρ^0 mesons, nor other known resonances cause the seagull effect in our data.

In order to investigate (i), we studied Monte Carlo events generated according to phase space weighted by $\Pi_{i=1}^{6} \exp(-Ap_{Ti})$ as described above. The curves in fig. 12 show that the results of these Monte Carlo studies agree well with the experimental data. For confirmation of this we studied $\langle p_T \rangle$ as a function of rapidity, and found both for the experimental data and Monte Carlo events that the seagull dip disappeared as expected for a purely p_T-limited phase space effect. For another confirmation we calculated, following Apeldoorn et al. [9], the energy weighted average p_T as a function of x, as shown in fig. 13. Again

the absence of a dip at small x is to be expected for a p_T-limited phase space effect. We conclude that the seagull effect in our data is satisfactorily explained by (i) alone.

5.4 Distribution of charge

We have made a detailed analysis of how the charge is spread in longitudinal rapidity using procedures proposed by Newmeyer and Sivers [10] and by Cahn and Colglazier [11]. The procedure is to make a cut in rapidity at some value, y_{cut}, and for each event sum the charges of those particles whose rapidity is less than y_{cut}, that is those whose rapidity is closer to the recoil proton. We then study how the moments, $\langle Q^n \rangle$, of this summed charge vary with y_{cut}, with 6π mass and with E_γ.

For a multiperipheral ladder produced by diffractive dissociation of the photon one would expect $\langle Q \rangle = 0$ everywhere. If, however, the distribution of particles were due to a multiperipheral ladder including the proton, local conservation of charge should cause $\langle Q \rangle$ to be less than zero for large negative y_{cut}. Measurements of $\langle Q \rangle$ are shown in fig. 14: they are in substantial agreement with the prediction for diffractive dissociation.

Figure 15 shows considerable variation of $\langle Q^2 \rangle$ with y_{cut} and with mass, but no variation with E_γ. We also see good symmetry between positive and negative y_{cut}, pointing again to forward-backward symmetry of the photon-Pomeron collision.

In detail $\langle Q^2 \rangle$ shows a change from a distribution at low mass which peaks at $y_{cut} = 0$ to a distribution which does not vary with y_{cut} at higher mass. The peaked distribution at low mass can be understood as due to a random arrangement of charges; as le Bellac [12] shows this would give

$$\langle Q^2 \rangle \propto K\left[1 - (y/y_{max})^2\right] .$$

The curve compared with the results for $2.0 < M_{6\pi} < 2.5$ GeV/c^2 in fig. 15 was calculated by the Monte Carlo method, assuming p_T-limited phase space and random assignments to the charges. The results of this calculation agree well with the low mass data in both shape and magnitude. A flat distribution of $\langle Q^2 \rangle$ as a function of y_{cut} can be understood as the result of a multiperipheral ladder in which no link transfers more than one unit of charge. A naive counting of possible arrangements of charge then predicts for this model a constant value of $\langle Q^2 \rangle \approx 0.6$, as discussed by Newmeyer and Sivers [10] and by Cahn and Colglazier [11].

5.5 Two-particle correlations

To obtain further information we compared the observed number of coincidences, N_C, between pairs of particles at rapidities y_1 and y_2, respectively, with the number N_R of coincidences expected from the single-particle distributions under the assumption of random coincidence. We calculated from the data

$$C = N_C - N_R \ ,$$

chosen so that non-zero values display non-random effects, and we show the results in fig. 16. There is forward-backward symmetry in the 6π c.m. system. All the results for equal charge pairs, together with those for opposite charge pairs at the lower masses, show positive long-range correlation at $y_1 \approx -y_2 \sim \pm 1.6$ and negative short-range correlation at $y_1 \sim y_2 \approx \pm 1.6$. The curves, from Monte Carlo calculation of p_T-limited phase space, reproduce these results in both shape and magnitude.

In contrast to these results, high-energy proton-proton collisions are known to result in strong short-range correlations, resulting from large contributions to the final state from meson resonances [13-15]. Any short-range correlation in our data, for example in pairs of oppositely charged particles, is certainly much less strong than in proton-proton collisions.

We note also that these results show no long-range correlation such as has been suggested [16,17] could occur in the dressing of a quark-antiquark jet.

6. JET ANALYSIS

The phenomenon of transverse momentum limitation relative to the beam axis is already well known in hadronic interactions and therefore, within the framework of VDM, would be expected in photoproduction. Transverse momentum limitation has also been observed in the jets produced in e^+e^- annihilation. In that case the jets are believed to originate from a quark-antiquark state. We therefore speculate on the possibility of a similar process contributing to our observations, and we compare our results with those from e^+e^- annihilation at SPEAR [18,19] and at DORIS [20].

Because of the similarity of jet systems with p_T-limited phase space, the only significant comparison we can make between our data and that from SPEAR and DORIS is in the degree by which the transverse momentum is truncated. Specifically we compare measurements of $\langle p_T \rangle$. The SPEAR measurements, which have been corrected for apparatus problems including uncertainty in determination of the jet axis [19], are shown in fig. 9 with our results; there is excellent agreement. The DORIS results [20] are measurements of the mean value of p_T with respect to the sphericity axis*): $\langle p_T \rangle_{sph}$. Our measurements of this quantity are shown in fig. 17, where they are compared with the results from DORIS [20]. Again the agreement is good.

We now consider the angular distribution of the jet axis. We define a jet axis as that direction along which the pion momentum vectors most nearly lie. We have used the sphericity axis [18,21] for this purpose, but have checked that

---

*) Our Monte Carlo calculations showed

$$\langle p_T \rangle_{sph} \Big/ \langle p_T \rangle_{true} \approx 0.75\text{-}0.85$$

for the p_T limitation found to fit our data. This ratio varied only slowly with mass of the hadronic system.

the use of thrust axis [22] makes no change to the conclusion. We have calculated the angular distribution of the sphericity axis with respect to the incident photon direction in the 6π c.m. system. The distribution is strongly peaked near zero angle, showing that the t-channel axis is significant for the process which produced these events. To confirm this point we examined the angular distribution of the sphericity axis with respect to the recoil proton direction in the 6π c.m. system (s-channel axis) and found it to be appreciably broader. Figure 18 shows the angular distributions with respect to the t-channel axis for the mass ranges:

$$2.75 < M_{6\pi} < 3.5 \ , \quad 3.5 < M_{6\pi} < 4.25 \ , \quad 4.25 < M_{6\pi} < 5.0$$

(with the selection of photon energies already described). It was checked before compiling fig. 18 that there was no observable dependence on the photon energy. The curves shown in fig. 18 are the distributions from our Monte Carlo calculations of the angle between sphericity axis and true axis. These curves are in substantial agreement with the data, showing that the jet axis is along the photon direction. We conclude therefore that if the jets have arisen from the materialization of the photon into a quark-antiquark pair, the quark-antiquark axis is aligned along the photon direction.

The consistency of the data with this quark-antiquark interpretation raises the interesting question as to whether such a quark-antiquark pair could originate from a point interaction of the photon, or from the well-known hadronic content of the photon responsible for the majority of the total cross-section. At present it is not possible to distinguish between these possibilities, since data of comparable detail to those presented here are not available from π^+ and π^- interactions in the 20-70 GeV range.

7. SUMMARY

i) In the reaction $\gamma p \to \pi^+\pi^-\pi^+\pi^-\pi^+\pi^- p$, there is a major contribution in which the six pions are produced by diffractive dissociation of the photon. This diffractive dissociation produces states with an essentially flat mass

spectrum from 2 to 5 GeV/c^2. Most of the pions are directly produced, the $\rho^0/\pi^\pm$ ratio being approximately 0.1.

ii) The pion transverse momentum with respect to the photon direction is limited. Specifically the distribution of momenta is found to be in good agreement with phase space weighted by $\Pi_{i=1}^{6}$ exp $(-Ap_{Ti})$, with A = 3.0-3.5.

iii) The structure of the 6π system shows several features, all of which vary with the 6π mass but not with the beam energy. The following features of the 6π system are well described by p_T-limited phase space:

a) $\langle p_T \rangle$ as a function of 6π mass,

b) rapidity and Feynman x distributions,

c) seagull effect,

d) two-particle correlations.

The charge distribution in rapidity indicates that for high mass states there is a dynamical effect on the charges in addition to the p_T-limited phase space affecting the momenta.

iv) The 6π state has a jet-like structure which is similar to that observed in hadronic states from e^+e^- annihilation. The jet axis is consistent with lying along the photon direction.

8. ACKNOWLEDGEMENTS

We are grateful to CERN for providing the facilities, and especially to the Omega Group for their help in operating the spectrometer, and the DD Division for providing on-line and off-line software. We have also benefited from the work of technical staff in our home institutions. We acknowledge financial support from the Science Research Council, from the Institut National de Physique Nucléaire et de Physique des Particules, and from the Bundesministerium für Wissenschaft und Forschung.

REFERENCES

[1] T.H. Bauer, R.D. Spital, D.R. Yennie and F.M. Pipkin, Rev. Mod. Phys. 50 (1978) 261.

[2] H.H. Bingham et al., Phys. Lett. 41B (1972) 635.

[3] F. Bourgeois, H. Grote, J.-C. Lassalle, Pattern recognition methods for Omega and SFM spark chamber experiments, CERN/DD/DH/101.
H. Grote, M. Hansroul, J.-C. Lassalle and P. Zanella, Identification of digitised particle trajectories, Proc. Internat. Computing Symposium, Davos, 1973 (North-Holland, Amsterdam 1974), p. 413.

[4] M.G. Albrow et al., Nucl. Phys. B108 (1976) 1.

[5] M.G. Albrow et al., Nucl. Phys. B102 (1976) 275.

[6] E.L. Berger and A. Krzywicki, Phys. Lett. 36B (1971) 380.

[7] A. Seiden, SLAC-PUB-1962 (1977).

[8] Y. Zarmi, Nucl. Phys. B134 (1978) 521.

[9] G.M. van Apeldoorn et al., Nucl. Phys. B91 (1975) 1.

[10] J.L. Newmeyer and D. Sivers, Phys. Rev. D9 (1974) 2592.

[11] R. Cahn and E. Colglazier, Phys. Rev. D9 (1974) 2658.

[12] M. le Bellac, CERN 76-14 (1976).

[13] A. Arneodo and G. Plaut, Nucl. Phys. B107 (1976) 262.

[14] A. Arneodo and G. Plaut, Nucl. Phys. B113 (1976) 156.

[15] C. Jancso et al., Nucl. Phys. B124 (1977) 1.

[16] J.D. Bjorken, SLAC-167 (1973) and SLAC-PUB-1756 (1976).

[17] S.J. Brodsky and N. Weiss, Phys. Rev. D16 (1977) 2325.

[18] G.G. Hanson et al., Phys. Rev. Lett. 35 (1975) 1609.

[19] G.G. Hanson, SLAC-PUB-2118 (1978) and Proc. 13th Rencontre de Moriond, Les Arcs, Savoie, France, March 1978 (Ed. Frontières, Dreux, 1978), p. 15.

[20] Ch. Berger et al., Phys. Lett. 78B (1978) 176 and 81B (1979) 410.

[21] J.D. Bjorken and S.J. Brodsky, Phys. Rev. D1 (1970) 1416.

[22] S. Brandt and H.D. Dahmen, Z. Phys. C1 (1979) 61.

Table 1

Mass cuts for the three photon energy ranges used in the analysis

Photon energy (GeV)	Mass (GeV/c^2)
25-35	< 3.5
35-50	< 4.25
50-70	< 5.0

Table 2

Values of b resulting from fitting t-distributions with A exp (bt)

Photon energy range (GeV)	6π mass range (GeV/c^2)	b
25-35	2-3	5.67 ± 0.50
35-50	2-3	5.32 ± 0.48
50-70	2-3	4.67 ± 0.56
35-50	3-4	5.40 ± 0.44
50-70	3-4	3.58 ± 0.44
50-70	4-5	4.78 ± 0.38

Figure captions

Fig. 1 : Schematic view of the photon tagging system. The incident electron of momentum 81.5 GeV/c is detected by the beam spectrometer before entering this system. An electron which radiates in the tungsten radiator is detected in the multiwire proportional chambers MWPC 1-4 and the hodoscopes HC1-2, while the photon produced travels on into the Omega spectrometer.

Fig. 2 : Plan view of the Omega spectrometer as equipped for this photoproduction experiment.

Fig. 3 : Number of events as a function of ΔE = incident photon energy - Σ (energies of observed charged particles) for events selected as the 6π sample with $2 < M_{6\pi} < 4$ GeV/c^2 and with incident photon energy between 35 and 65 GeV. The steep rise at $\Delta E \approx -0.5$ GeV indicates one side of the elastic peak, the other side of which merges into the inelastic distribution. This inelastic distribution is indicated by the curve, and has been estimated as described in the text.

Fig. 4 : Acceptances for detecting 6π candidates from the reaction

$$\gamma + p \rightarrow p + (X \rightarrow \pi^+\pi^-\pi^+\pi^-\pi^+\pi^-)$$

as a function of mass of X for three photon energies:
——— E_γ = 30 GeV, - - - - E_γ = 42.5 GeV, -.-.-.- E_γ = 60 GeV,
as calculated with the Monte Carlo program described in section 3 of the text. The curves which fall with increasing mass show the fractions of events which were detected with all six pions identified correctly, while the curves which rise with increasing mass show the fractions of events where at least three positive and three negative particles were detected, but with the proton identified as one of the six pions.

Fig. 5 : Experimental 6π mass spectra for three different ranges of photon energy.

Fig. 6 : Experimental t distributions, where t is the four-momentum transfer with which the 6π system is produced, for ranges of 6π mass and photon energy. The relative normalization has been adjusted to correspond to the same total numbers of events in each case, to facilitate comparisons. The results of exponential fits to these data are given in table 2.

Fig. 7a) : Observed mass spectrum for $\pi^+\pi^-$ pairs.

b) : Observed mass spectrum for $\pi^\pm\pi^\pm$ pairs.

Fig. 8 : A sample p_T distribution, dN/dp_T^2, as a function of p_T, for events with 6π mass between 3.5 and 4.25 GeV/c^2 and incident photon energy between 35 and 70 GeV. The results have been selected for three ranges of $x = p_L/p_{Lmax}$; $-0.5 < x < -0.1$, $0.1 < x < 0.1$, $0.1 < x < 0.5$. The results for $-0.1 < x < 0.1$ have been displaced upwards for clarity. p_L and p_T are defined with respect to the photon direction in the 6π rest system. The curves are calculated assuming phase space weighted by the factors:
——— $\Pi_{i=1}^6 \exp(-3.5\, p_{Ti})$, - - - $\Pi_{i=1}^6 \exp(-4.5\, p_{Ti}^2)$.

Fig. 9 : Experimental values of $\langle p_T \rangle$, the average of p_T of the six pions with respect to the photon direction in the 6π rest system, as a function of mass of the 6π system, for three ranges of incident photon energy: $25 < E_\gamma < 35$ GeV, $35 < E_\gamma < 50$ GeV, $50 < E_\gamma < 70$ GeV (data from this experiment); and SPEAR results. The curves show behaviour expected for phase space and for phase space weighted by $\Pi_{i=1}^6 \exp(-Ap_{Ti})$ or $\Pi_{i=1}^6 \exp(-Bp_{Ti}^2)$; the values of A or B are marked on the curves.

Fig. 10 : Pion longitudinal rapidity distributions with respect to the incident photon in the 6π rest system, for ranges of 6π mass. The normalization is to unit area. The curves are calculated assuming phase space weighted by $\Pi_{i=1}^{6} \exp(-Ap_{Ti})$, with A = 3.0 for the two lower masses and A = 3.5 for the two higher masses.

Fig. 11 : Distributions of numbers of pions as a function of $x = p_L/p_{Lmax}$ with respect to the incident photon in the 6π rest system for ranges of 6π mass and for ranges of incident photon energy: $25 < E_\gamma < 35$ GeV, $35 < E_\gamma < 50$ GeV, $50 < E_\gamma < 70$ GeV. The curves are calculated assuming phase space weighted by $\Pi_{i=1}^{6} \exp(-Ap_{Ti})$ with A = 3.0 for the two lower masses and A = 3.5 for the two higher masses.

Fig. 12 : Values of $\langle p_T \rangle$ as a function of $x = p_L/p_{Lmax}$, with p_T and p_L determined with respect to the incident photon direction in the 6π rest system. The curves are calculated assuming phase space weighted by $\Pi_{i=1}^{6} \exp(-Ap_{Ti})$, with A = 3.0 for the two lower masses and A = 3.5 for the two higher masses.

Fig. 13 : Experimental values of the energy-weighted average p_T, $\sum E_i p_{Ti} / \sum E_i$, plotted as a function of $x = p_L/p_{Lmax}$, where all these variables are defined in the 6π rest system with the momentum components being with respect to the incident photon direction.

Fig. 14 : Values of the average charge, on one side of a longitudinal rapidity y_{cut} (defined with respect to the incident photon direction in the 6π rest system) plotted as a function of y_{cut}, 6π mass and incident photon energy: $25 < E_\gamma < 35$ GeV, $35 < E_\gamma < 50$ GeV, $50 < E_\gamma < 70$ GeV.

Fig. 15 : Values of the average of the square of the total charge on one side of a longitudinal rapidity, y_{cut} (defined with respect to the incident photon direction in the 6π rest system) plotted as a function of y_{cut}, 6π mass and incident photon energy: ◇ $25 < E_\gamma < 35$ GeV, ✱ $35 < E_\gamma < 50$ GeV, ■ $50 < E_\gamma < 70$ GeV.

Fig. 16 : Values of $C = (N_C - N_R)/(\text{total number of coincidences})$. Here N_C is the observed number of coincidences per unit range of rapidities between a pair of particles: one with rapidity y_1, and the other with rapidity y_2. N_R is the corresponding number of coincidences one would deduce from the observed single-particle distributions if the probability of coincidence were random:

a) $2.0 < M_{6\pi} < 2.75$ GeV/c^2;

b) $2.75 < M_{6\pi} < 3.5$ GeV/c^2;

c) $3.5 < M_{6\pi} < 4.25$ GeV/c^2, equal charge pairs;

d) $3.5 < M_{6\pi} < 4.25$ GeV/c^2, opposite charge pairs;

e) $4.25 < M_{6\pi} < 5.0$ GeV/c^2, equal charge pairs;

f) $4.25 < M_{6\pi} < 5.0$ GeV/c^2, opposite charge pairs.

The symbols denote: ◇ $0.4 < y_1 < 2.0$, equal charge pairs, ✱ $-2.0 < y_1 < -0.4$, equal charge pairs, ■ $0.4 < y_1 < 2.0$, opposite charge pairs, ▲ $-2.0 < y_1 < -0.4$, opposite charge pairs. The curves are calculated assuming p_T-truncated phase space: ——— $0.4 < y_1 < 2.0$, - - - - $-2.0 < y_1 < -0.4$.

Fig. 17 : Values of $\langle p_T \rangle_{sph}$, the average value of p_T with respect to the sphericity axis in the 6π rest system as a function of 6π mass and for three ranges of incident photon energy: ◇ $25 < E_\gamma < 35$ GeV, ✱ $35 < E_\gamma < 50$ GeV, ■ $50 < E_\gamma < 70$ GeV. Also shown are corresponding measurements from jets from electron-positron annihilation, for data of all multiplicities and uncorrected for detector apertures: Δ DORIS [20].

Fig. 18 : Experimental distribution of the angle between the sphericity axis and the incident photon direction in the 6π rest system for three ranges of 6π mass:

a) $2.75 < M_{6\pi} < 3.5$ GeV/c^2,

b) $3.5 < M_{6\pi} < 4.25$ GeV/c^2,

c) $4.25 < M_{6\pi} < 5.0$ GeV/c^2.

The curves are calculated assuming p_T-limited phase space, as described in the text.

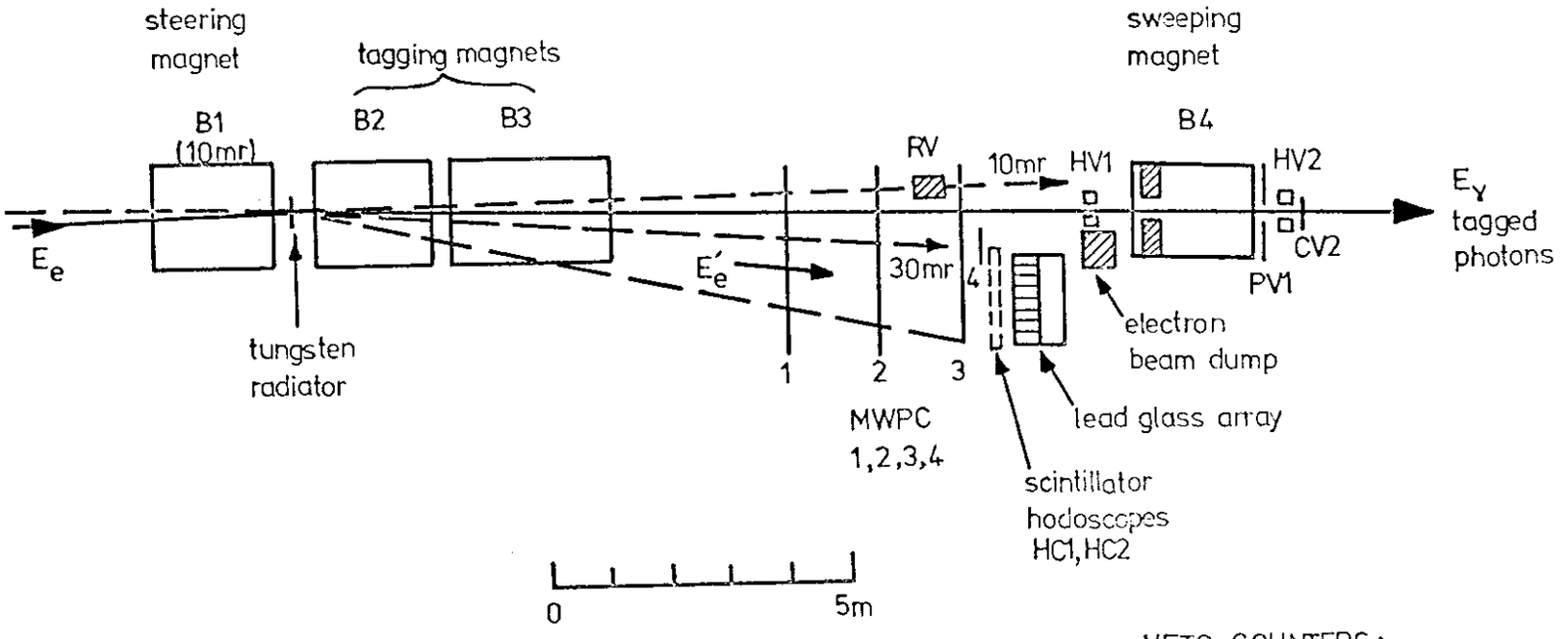
steering magnet
tagging magnets
sweeping magnet
B1 (10mr)
B2
B3
B4
RV
10mr
HV1
HV2
CV2
PV1
E_e
E'_e
30mr
E_γ tagged photons
tungsten radiator
1
2
3
4
MWPC 1,2,3,4
electron beam dump
lead glass array
scintillator hodoscopes HC1, HC2
0
5m
$E_\gamma = E_e - E'_e$
VETO COUNTERS:
RV upstream radiation
HV photon beam halo
PV, CV charged particle

Fig. 1

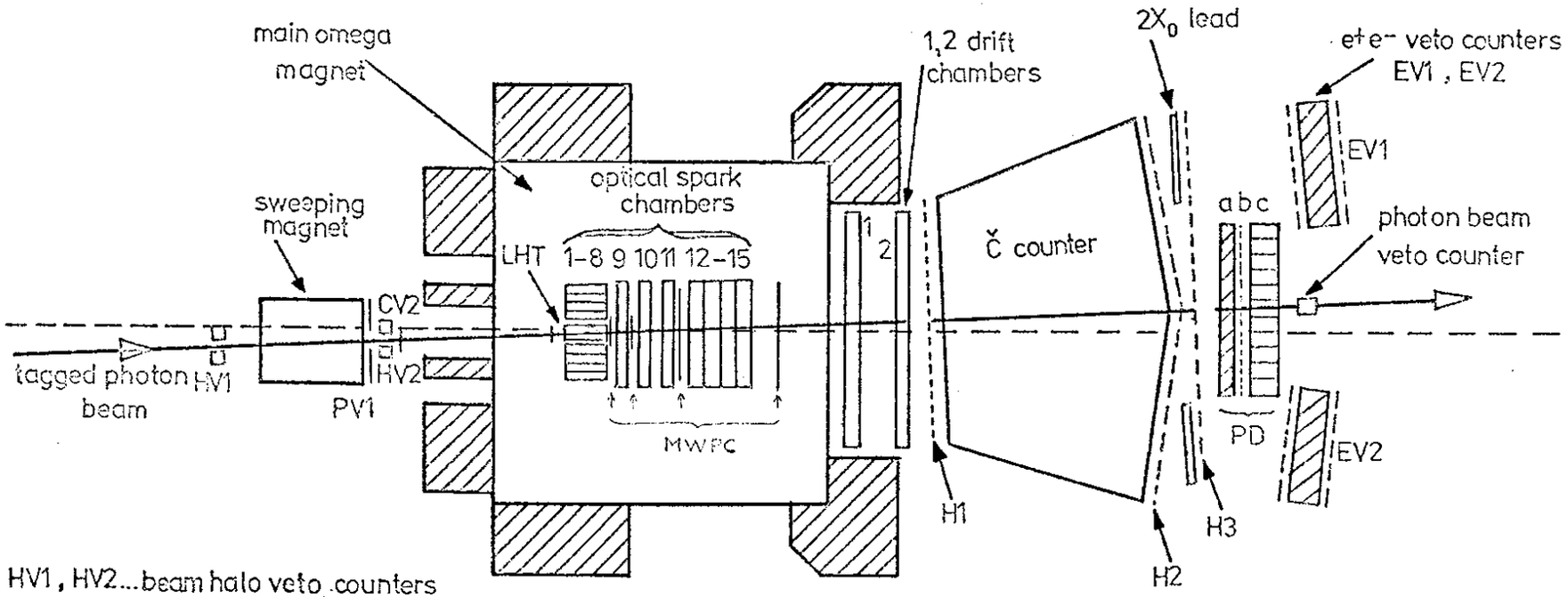

HV1 , HV2...beam halo veto counters

PV1 , CV2...charged particle veto counter

LHT.....liquid hydrogen target surrounded by scintillator array

H1 , H2 , H3..scintillator hodoscopes

PD PHOTON DETECTOR

a) lead glass shower sampler

b) scintillator hodoscopes

c) lead glass array

Fig. 2

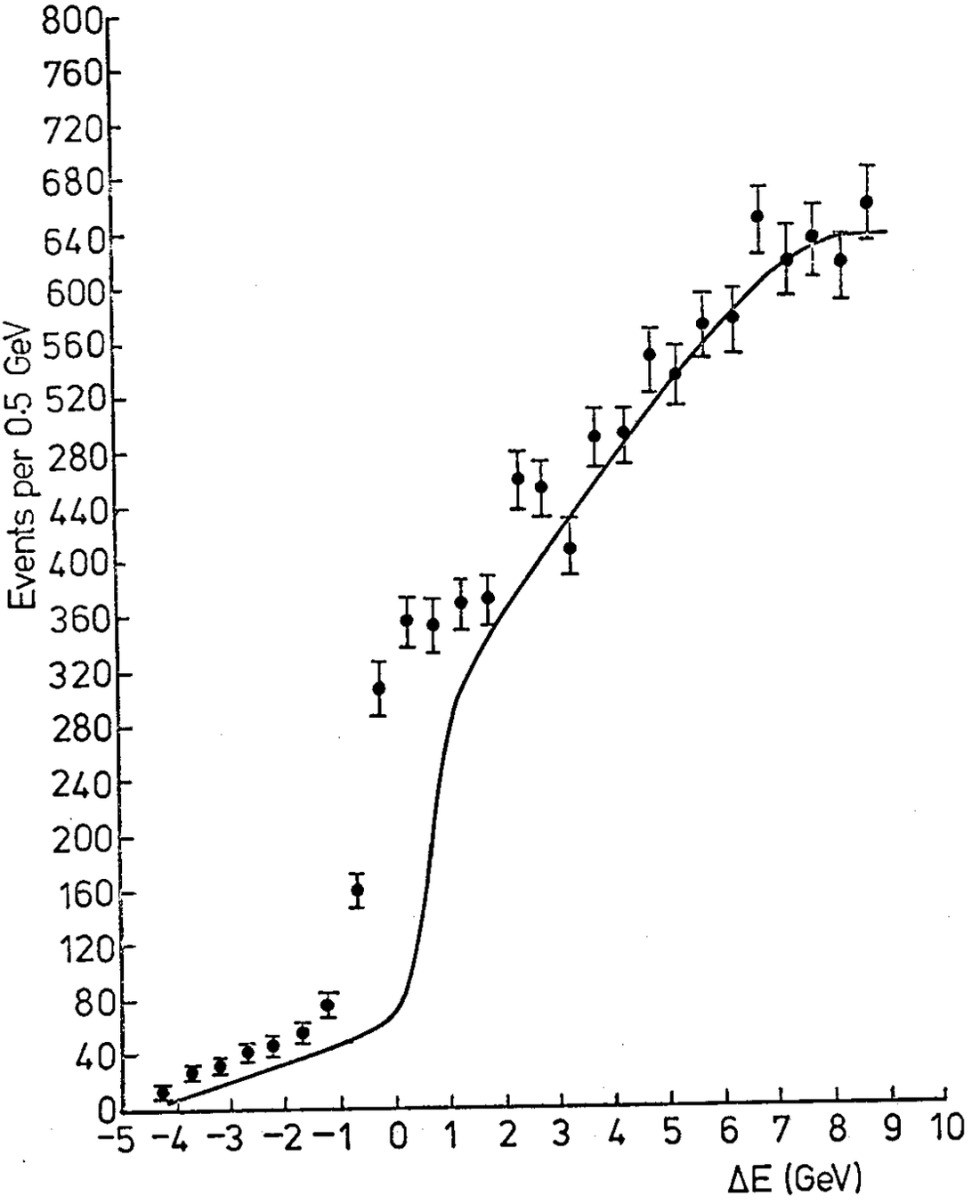
Events per 0.5 GeV
800
760
720
680
640
600
560
520
280
440
400
360
320
280
240
200
160
120
80
40
0
-5 -4 -3 -2 -1 0 1 2 3 4 5 6 7 8 9 10
ΔE (GeV)

Fig. 3

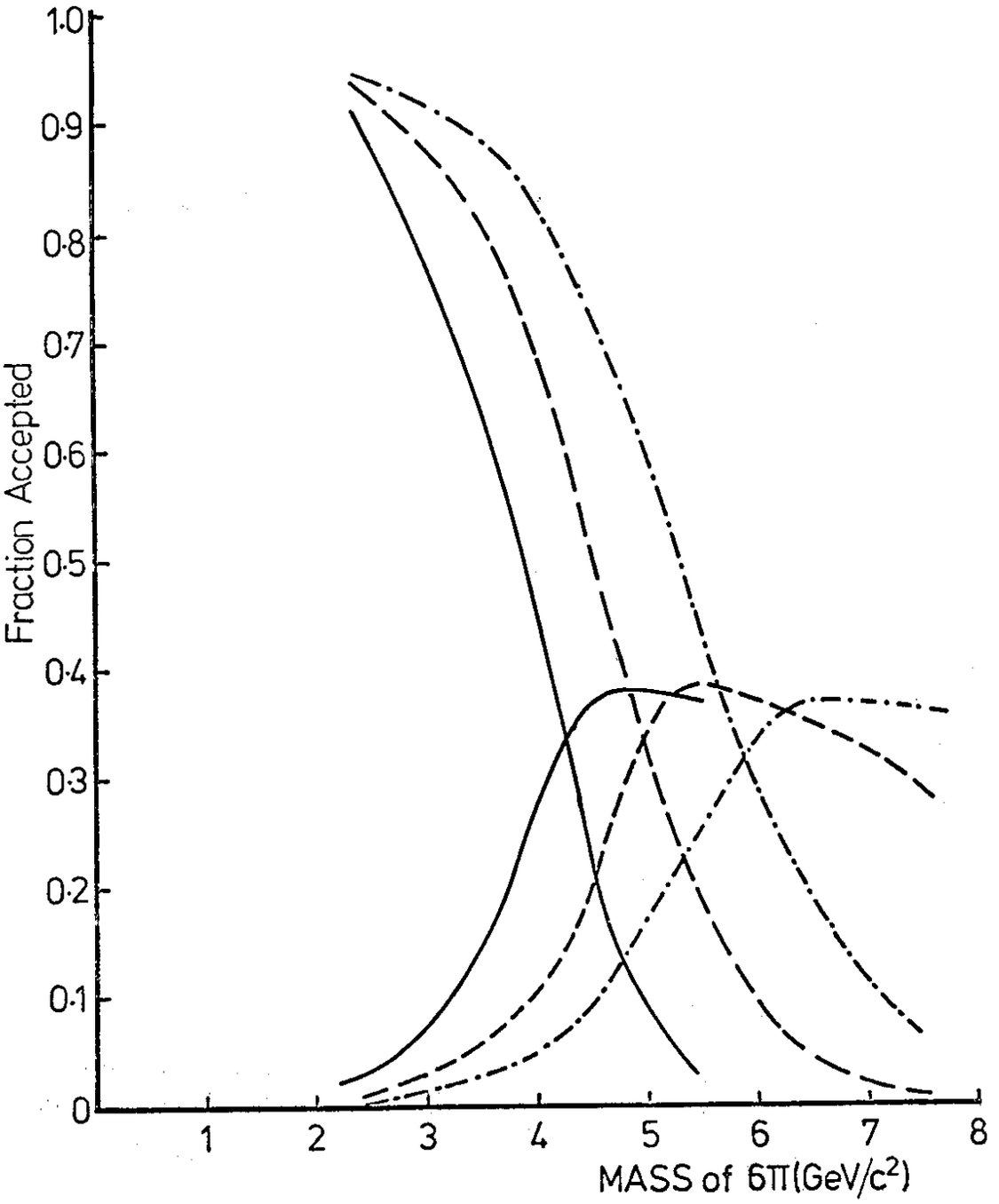
1·0
0·9
0·8
0·7
0·6
0·5
0·4
0·3
0·2
0·1
0
Fraction Accepted
1
2
3
4
5
6
7
8
MASS of 6π(GeV/c²)

Fig. 4

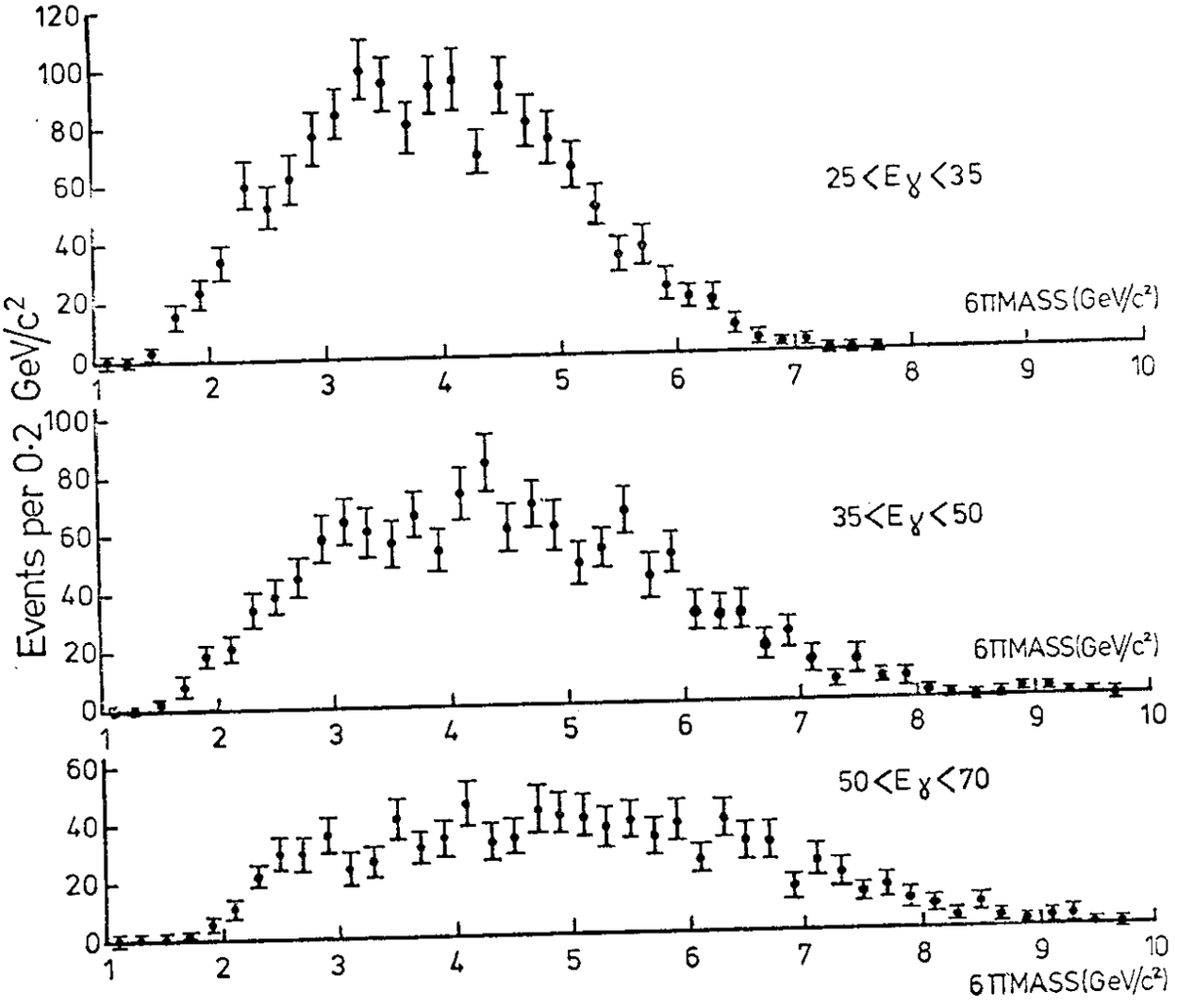
Events per 0·2 GeV/c²
25<Eγ<35
35<Eγ<50
50<Eγ<70
6πMASS(GeV/c²)
6πMASS(GeV/c²)
6πMASS(GeV/c²)

Fig. 5

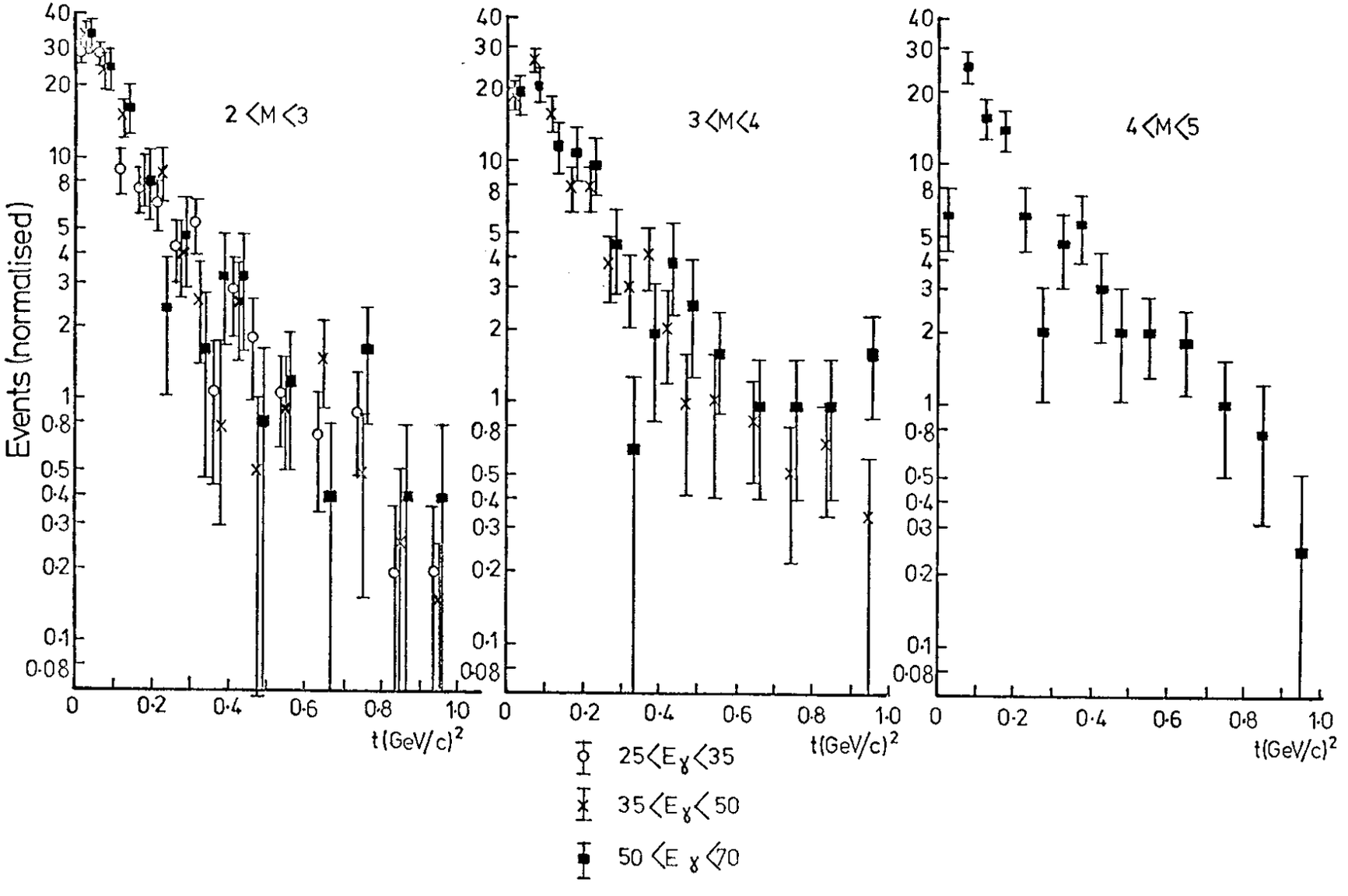

Fig. 6

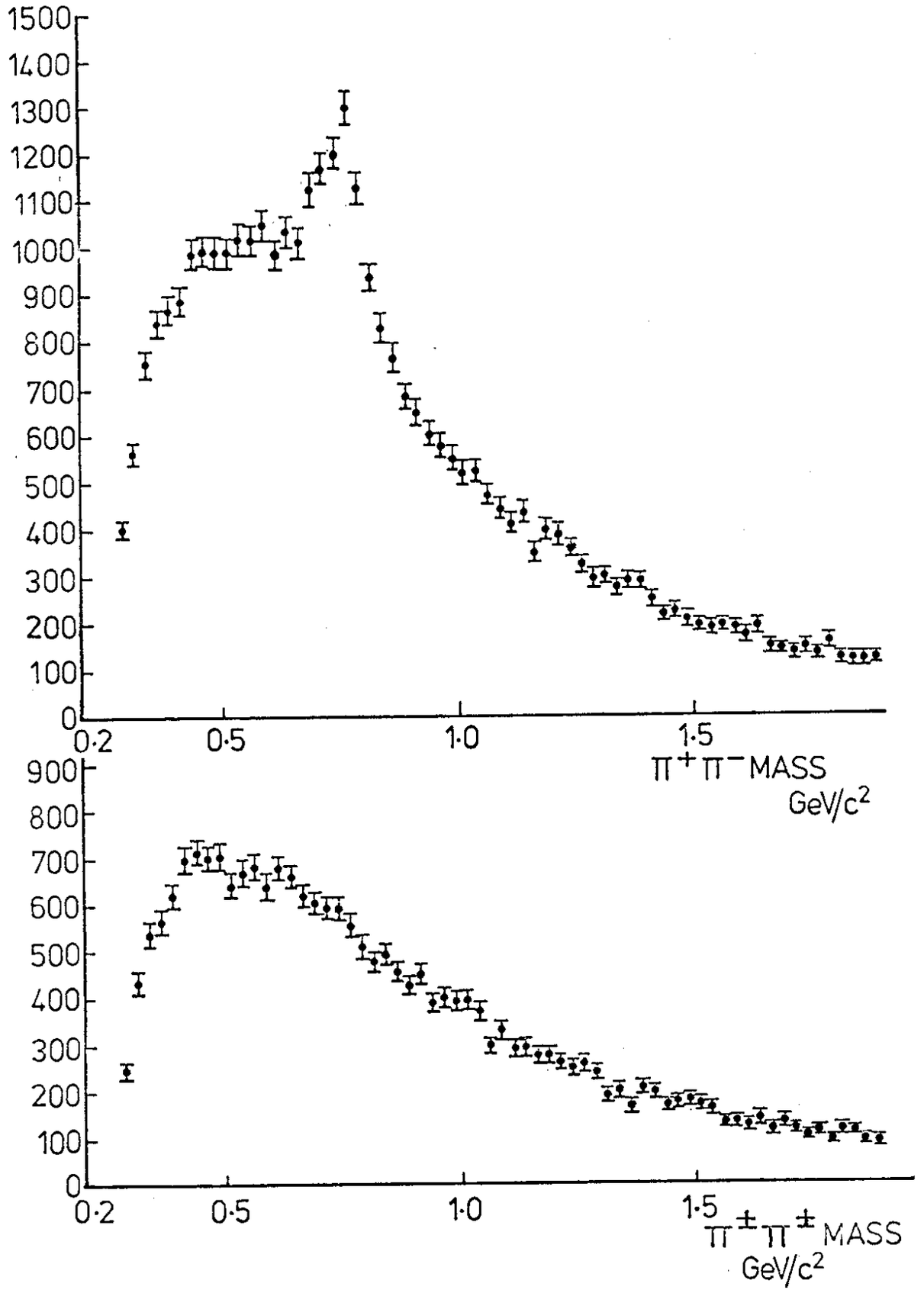
1500
1400
1300
1200
1100
1000
900
800
700
600
500
400
300
200
100
0
0·2
0·5
1·0
1·5
π+π− MASS
GeV/c²
900
800
700
600
500
400
300
200
100
0
0·2
0·5
1·0
1·5
π±π± MASS
GeV/c²

Fig. 7

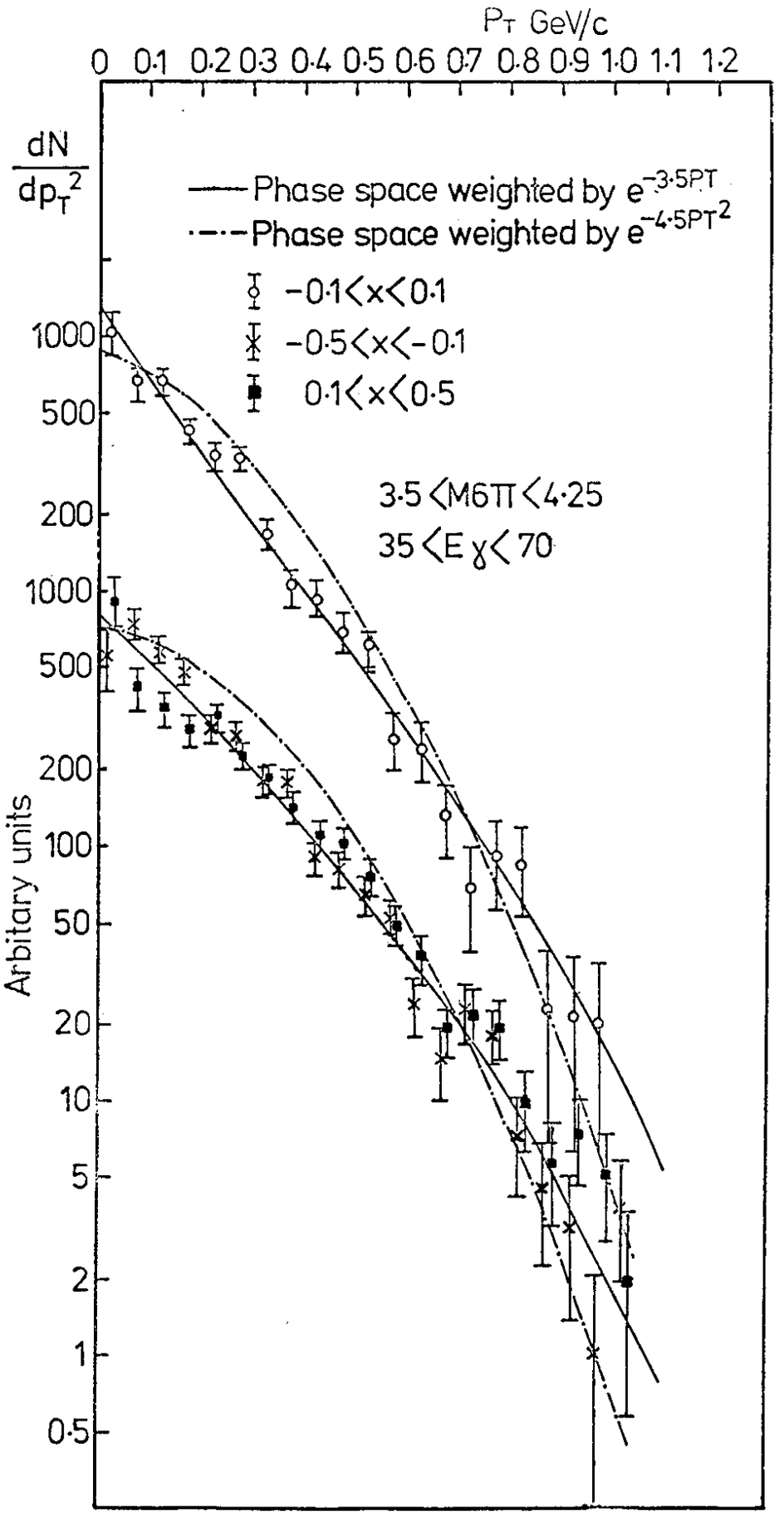
P_T GeV/c
0 0·1 0·2 0·3 0·4 0·5 0·6 0·7 0·8 0·9 1·0 1·1 1·2
$\frac{dN}{dp_T^2}$
Phase space weighted by $e^{-3·5PT}$
Phase space weighted by $e^{-4·5PT^2}$
$-0·1<x<0·1$
$-0·5<x<-0·1$
$0·1<x<0·5$
$3·5<M6\pi<4·25$
$35<E\gamma<70$
Arbitary units
1000
500
200
1000
500
200
100
50
20
10
5
2
1
0·5

Fig. 8

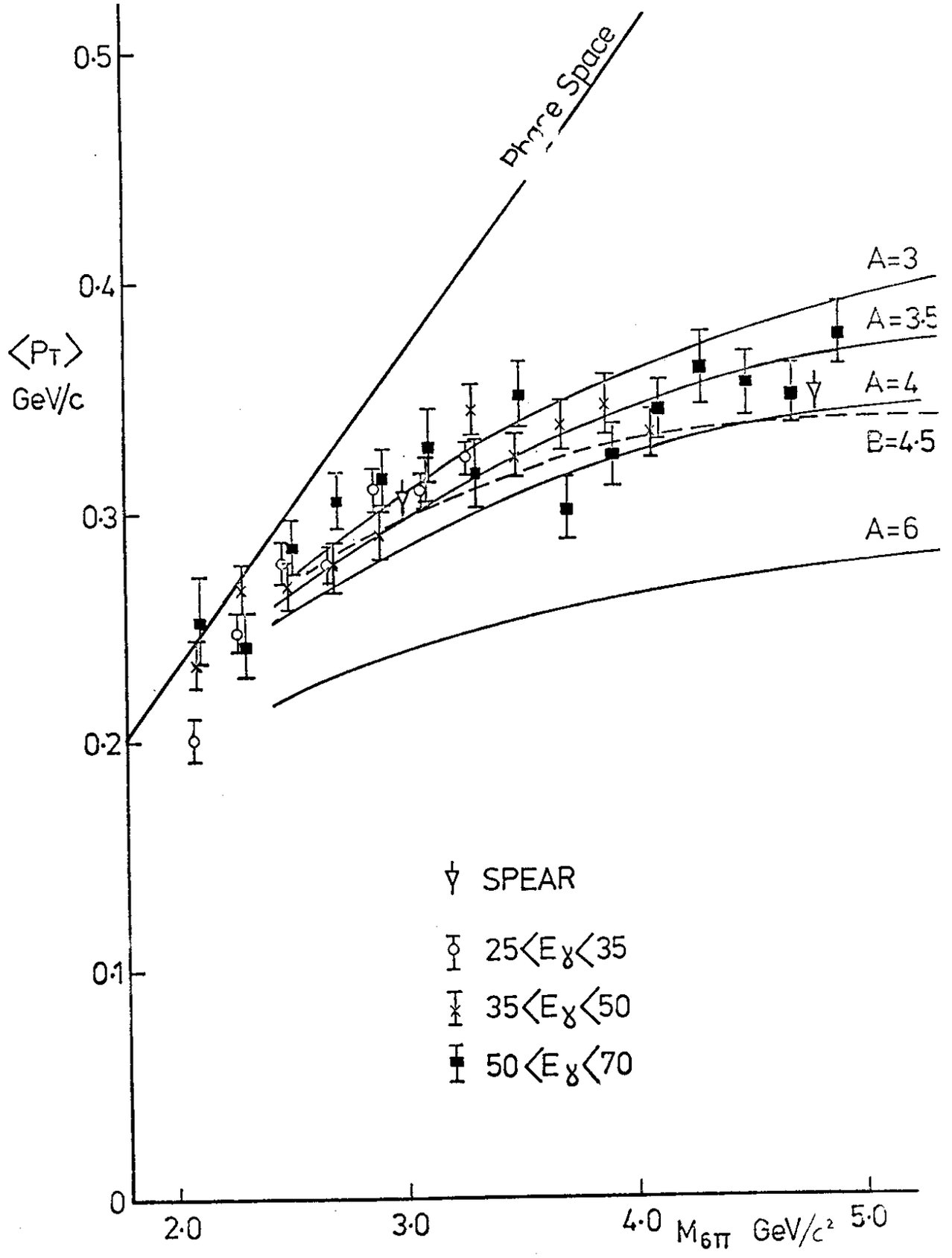
0·5
0·4
0·3
0·2
0·1
0
⟨PT⟩
GeV/c
Phase Space
A=3
A=3·5
A=4
B=4·5
A=6
SPEAR
25<Eγ<35
35<Eγ<50
50<Eγ<70
2·0
3·0
4·0
5·0
M6π GeV/c²

Fig. 9

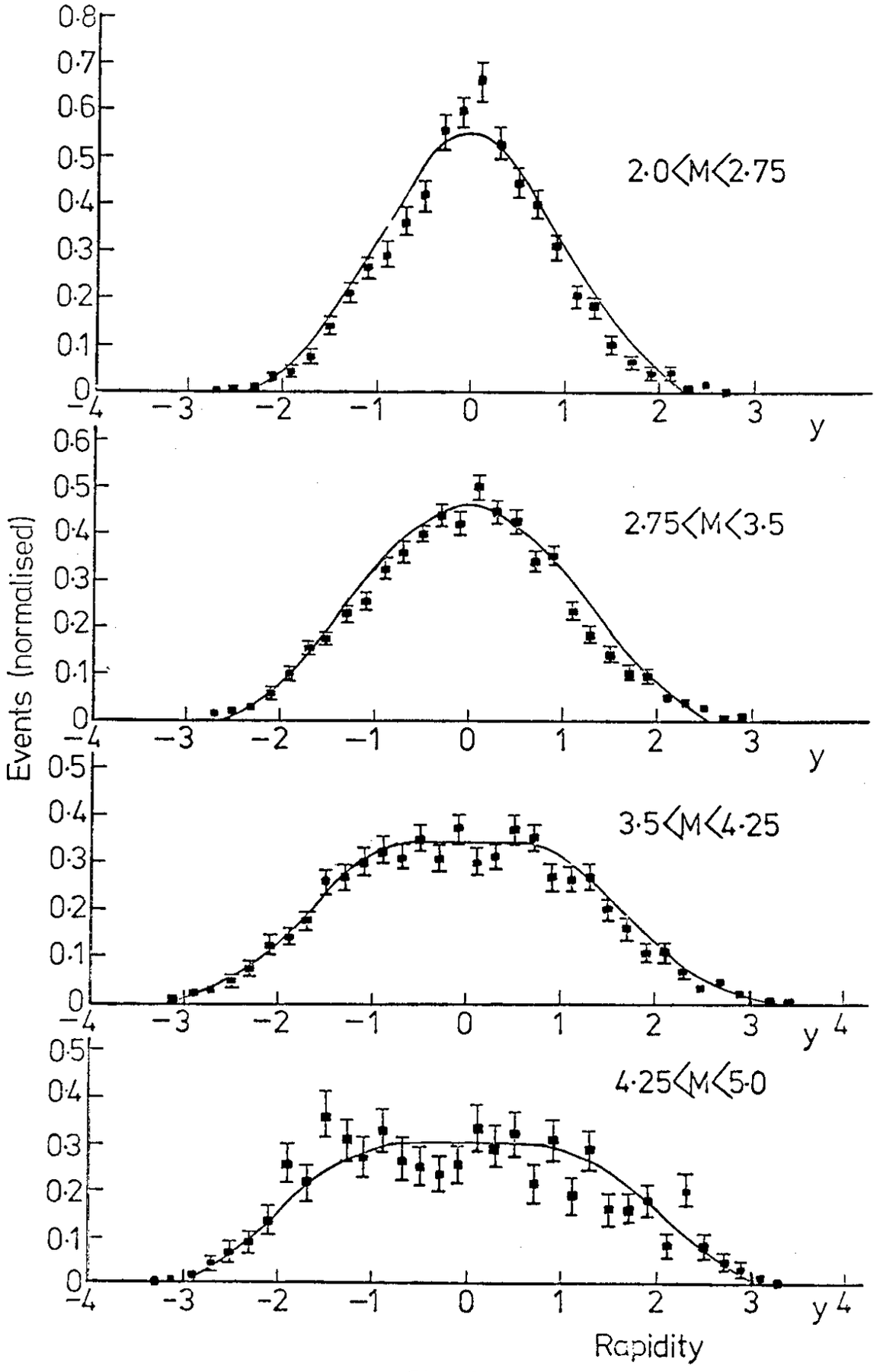

Fig. 10

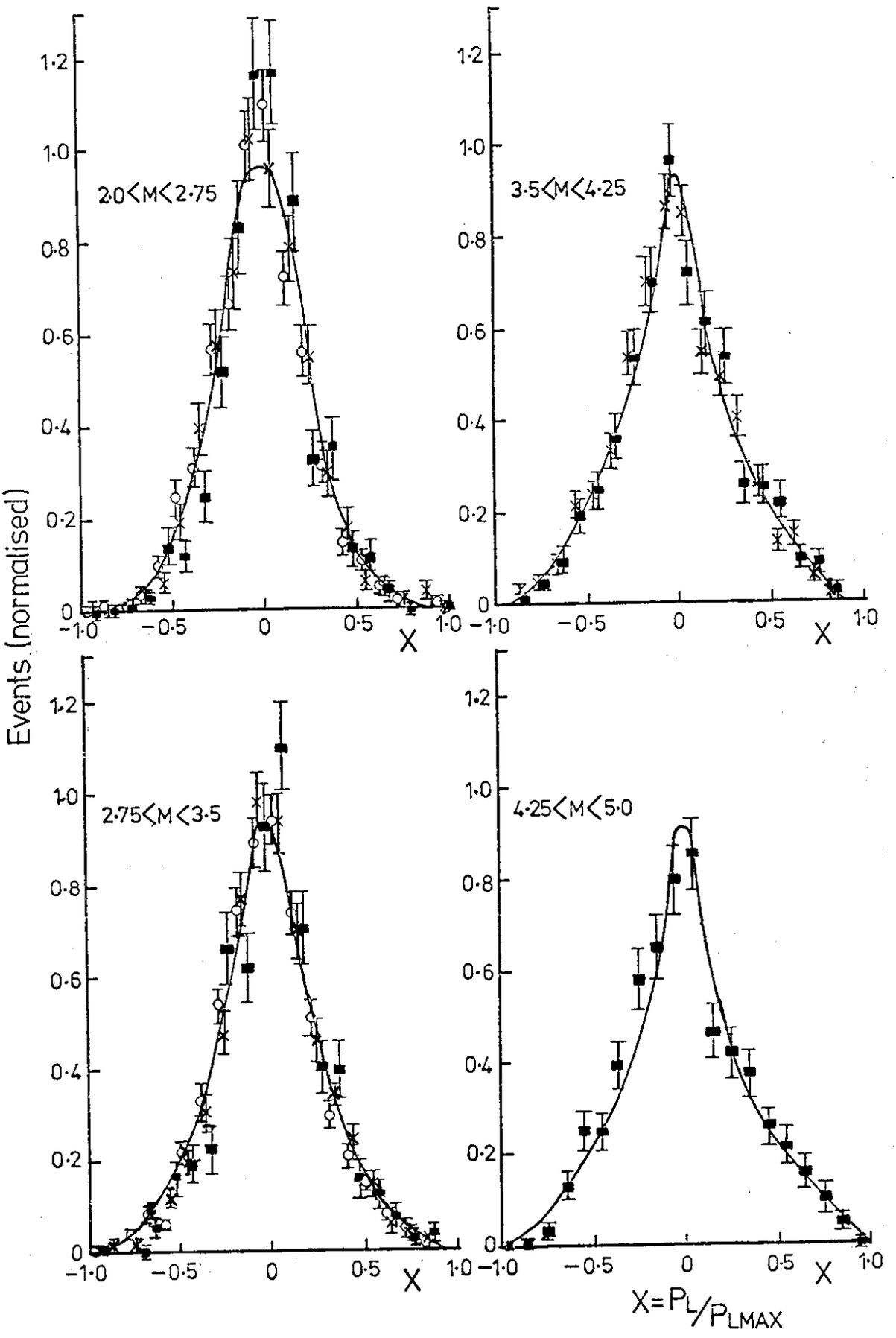

Fig. 11

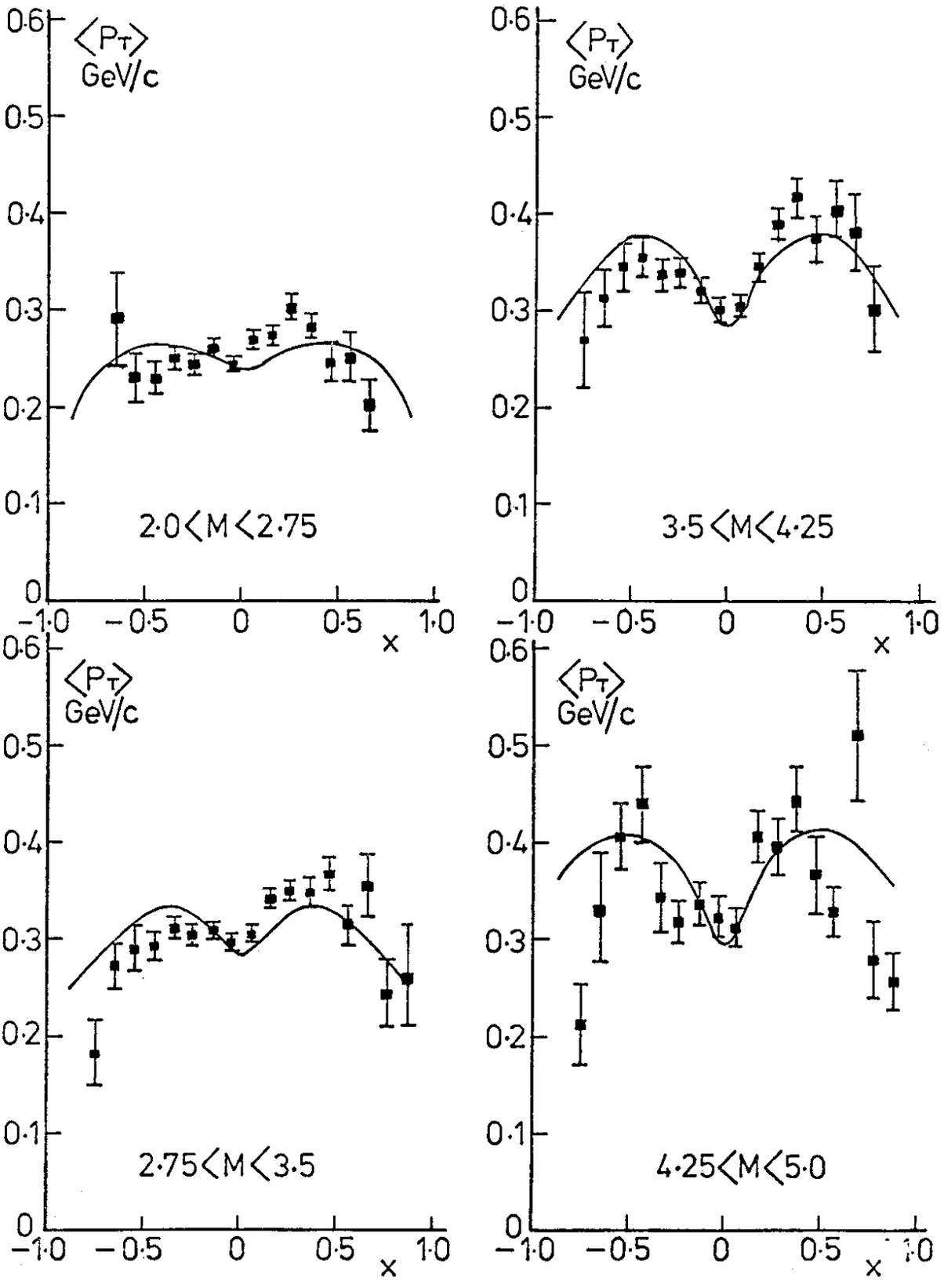

Fig. 12

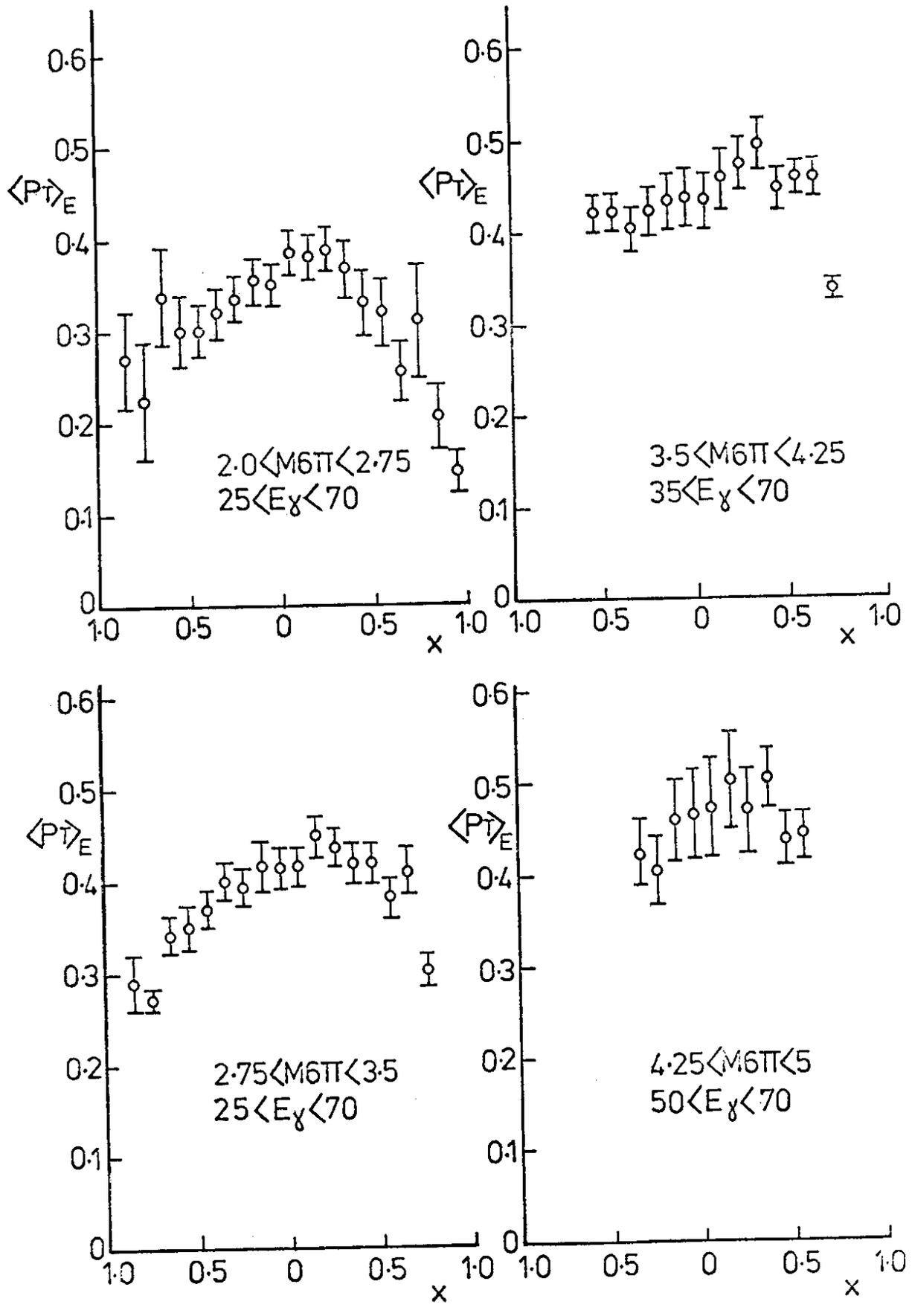
0·6
0·5
⟨PT⟩E
0·4
0·3
0·2
0·1
0
1·0
0·5
0
0·5
1·0
x
2·0<M6π<2·75
25<Eγ<70
3·5<M6π<4·25
35<Eγ<70
2·75<M6π<3·5
25<Eγ<70
4·25<M6π<5
50<Eγ<70

Fig. 13

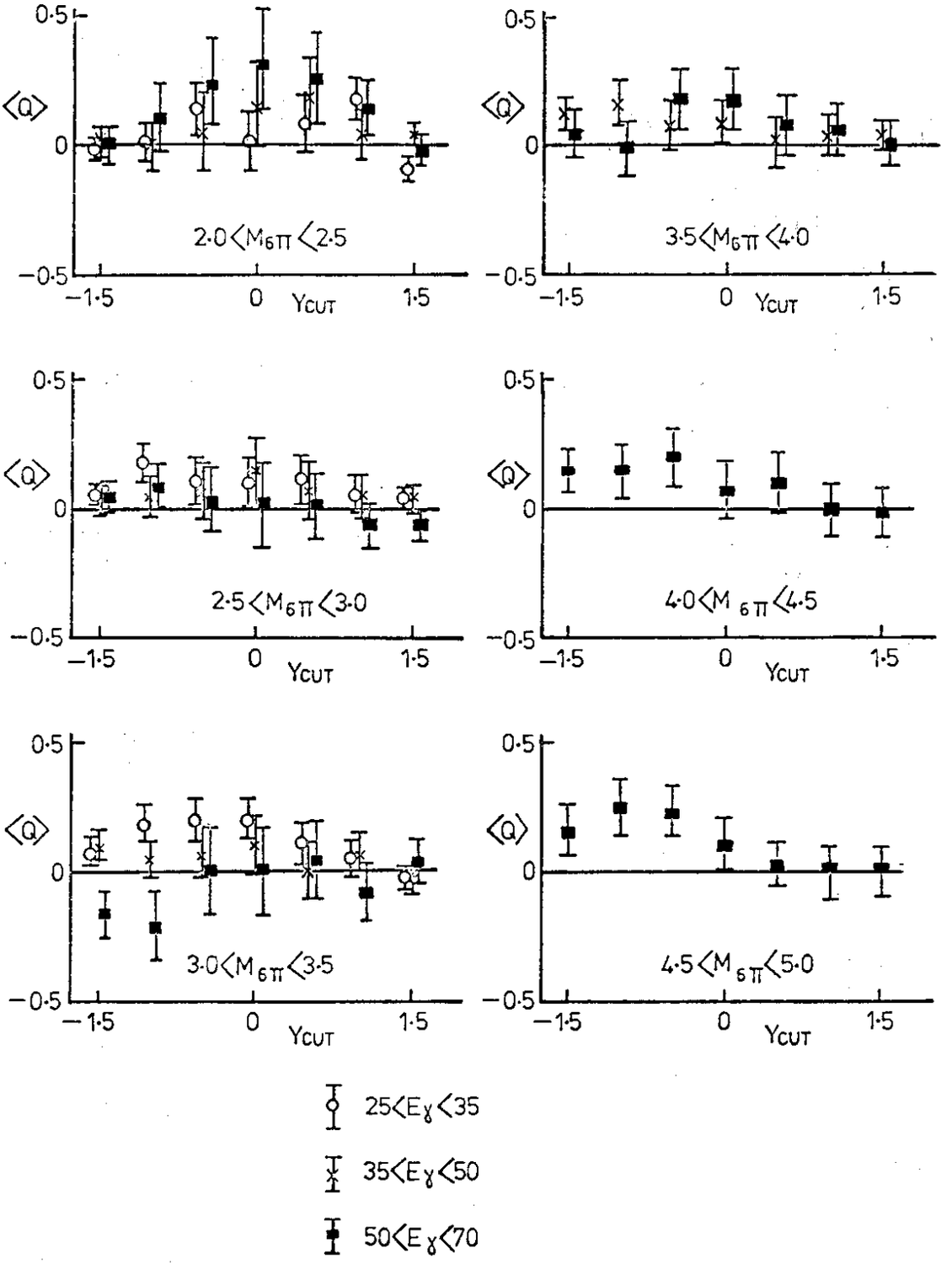
0·5
⟨Q⟩
0
−0·5
2·0<M6π<2·5
3·5<M6π<4·0
2·5<M6π<3·0
4·0<M 6π<4·5
3·0<M6π<3·5
4·5<M 6π<5·0
−1·5
0
YCUT
1·5
25<Eγ<35
35<Eγ<50
50<Eγ<70

Fig. 14

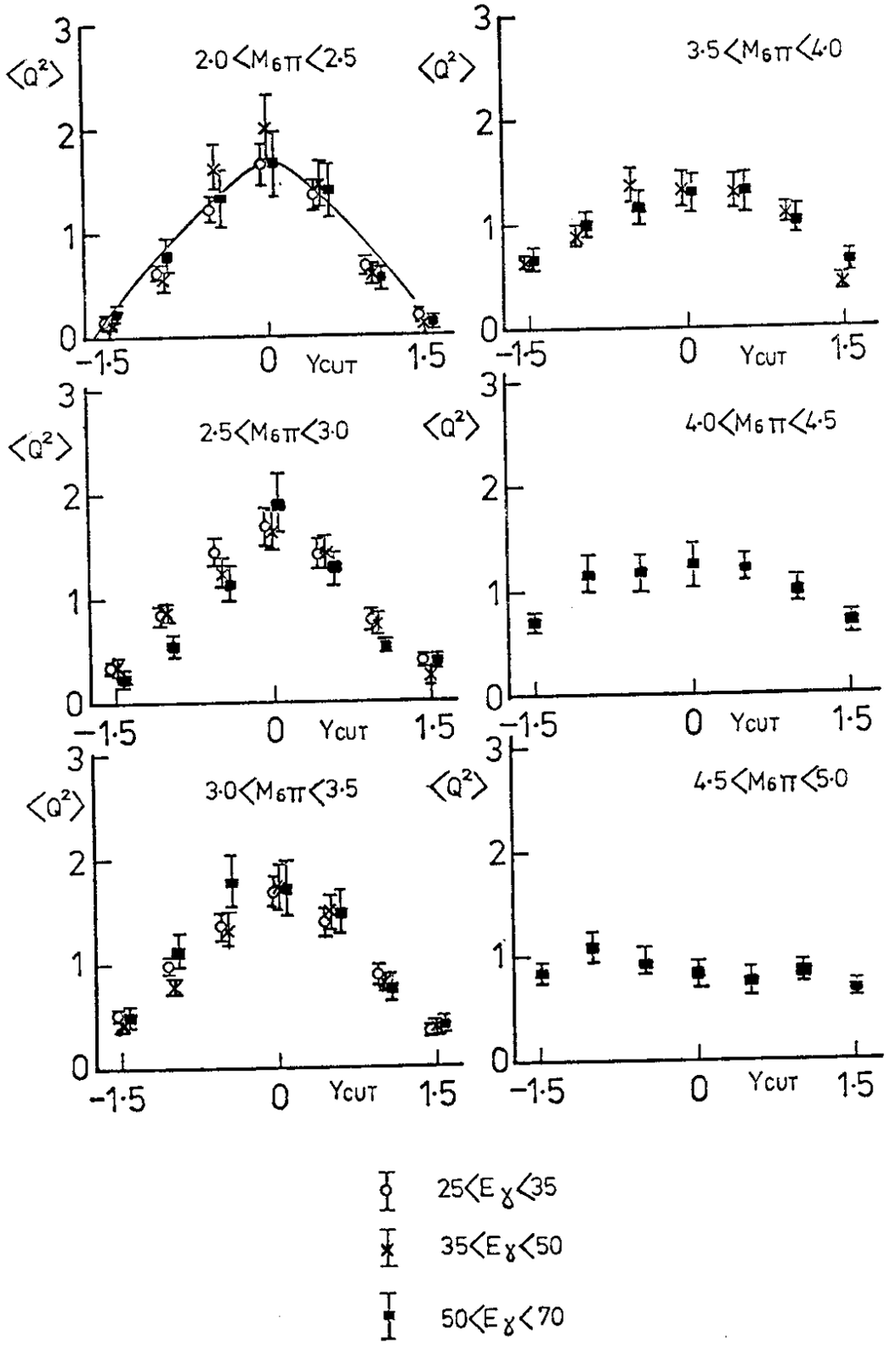
2·0<M6π<2·5
3·5<M6π<4·0
2·5<M6π<3·0
4·0<M6π<4·5
3·0<M6π<3·5
4·5<M6π<5·0
⟨Q²⟩
YCUT
−1·5
0
1·5
25<Eγ<35
35<Eγ<50
50<Eγ<70

Fig. 15

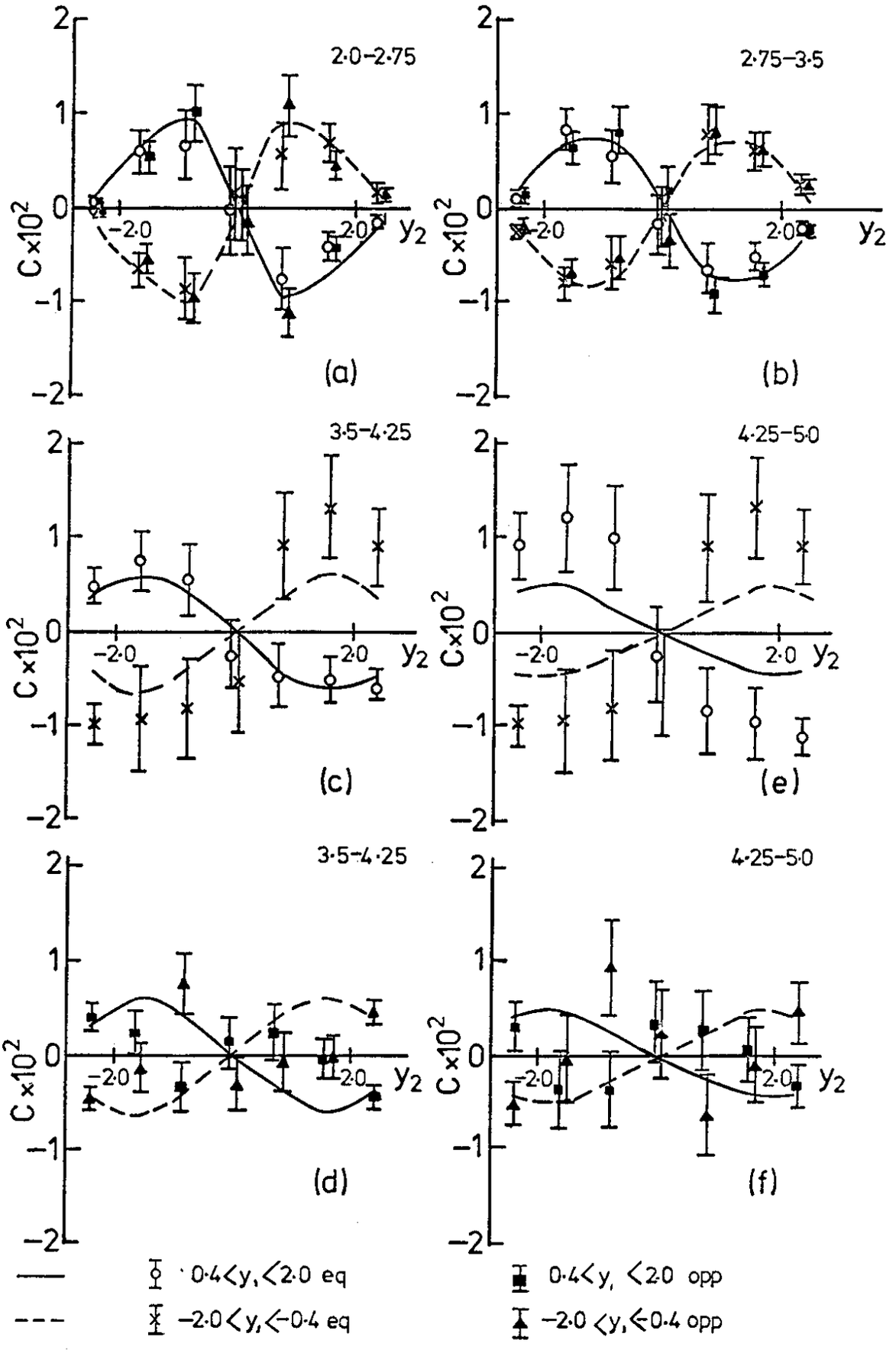
2·0–2·75
2·75–3·5
3·5–4·25
4·25–5·0
3·5–4·25
4·25–5·0
C×10²
y₂
(a)
(b)
(c)
(e)
(d)
(f)
0·4<y,<2·0 eq
−2·0<y,<−0·4 eq
0·4<y,<2·0 opp
−2·0<y,<−0·4 opp

Fig. 16

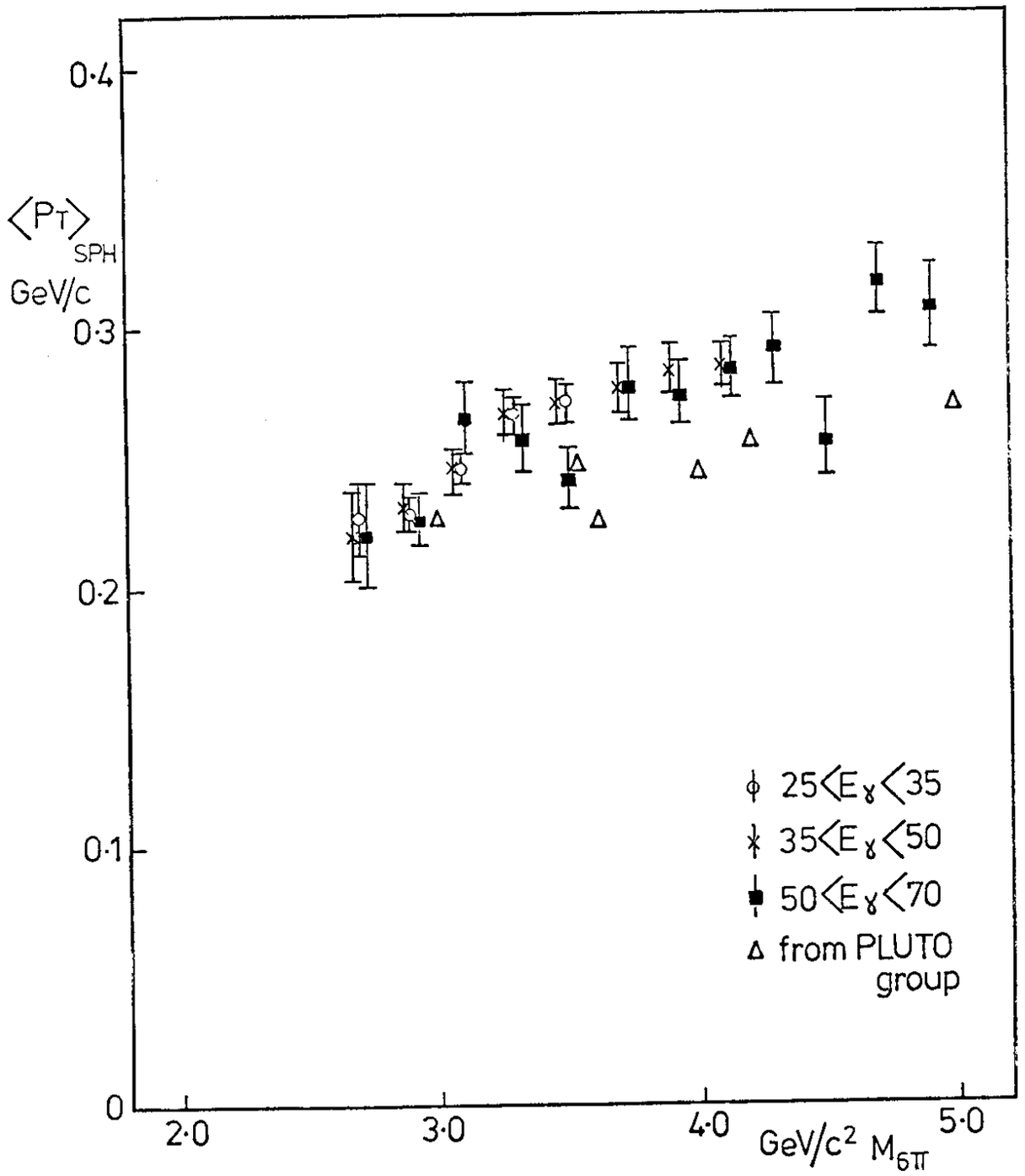
0·4
0·3
0·2
0·1
0
⟨PT⟩ SPH
GeV/c
2·0
3·0
4·0
5·0
GeV/c² M6π
25<Eγ<35
35<Eγ<50
50<Eγ<70
from PLUTO group

Fig. 17

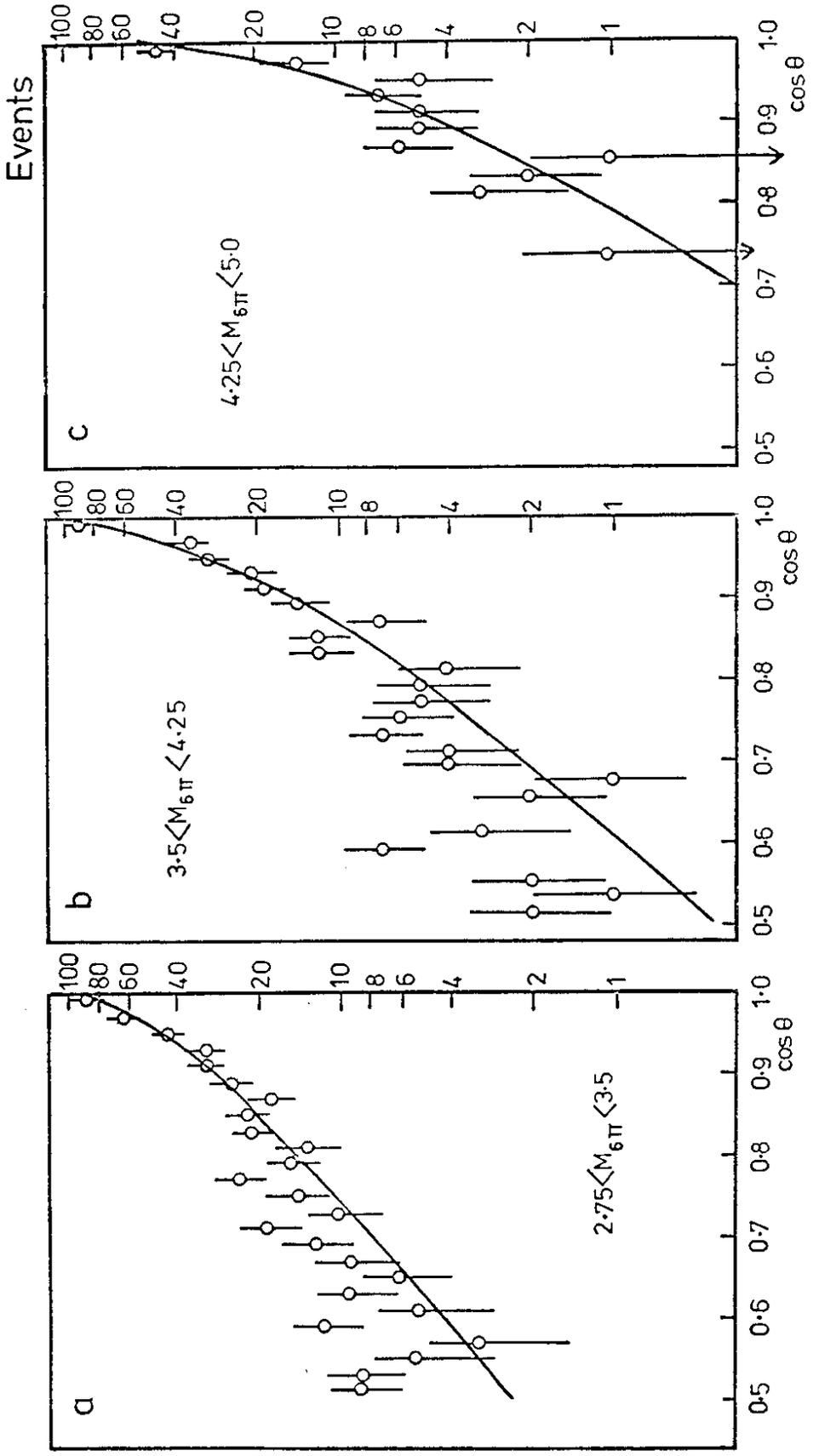
Events
a
b
c
2·75<M6π<3·5
3·5<M6π<4·25
4·25<M6π<5·0
cos θ
100
80
60
40
20
10
8
6
4
2
1
0·5
0·6
0·7
0·8
0·9
1·0

Fig. 18